J. Fluid Mech. (2010), *vol.* 642, *pp.* 95–125. © Cambridge University Press 2009
doi:10.1017/S0022112009991741

Passive and active bodies in vortex-street wakes

SILAS ALBEN†
School of Mathematics, Georgia Institute of Technology, Atlanta, GA 30332-0160, USA

(Received 6 February 2009; revised 14 August 2009; accepted 14 August 2009;
first published online 2 December 2009)

We model the swimming of a finite body in a vortex street using vortex sheets distributed along the body and in a wake emanating from its trailing edge. We determine the magnitudes and distributions of vorticity and pressure loading on the body as functions of the strengths and spacings of the vortices. We then consider the motion of a flexible body clamped at its leading edge in the vortex street as a model for a flag in a vortex street and find alternating bands of thrust and drag for varying wavenumber. We consider a flexible body driven at its leading edge as a model for tail-fin swimming and determine optimal motions with respect to the phase between the body's trailing edge and the vortex street. For short bodies maximizing thrust or efficiency, we find maximum deflections shifted in phase by 90° from oncoming vortices. For long bodies, leading-edge driving should reach maximum amplitude when the vortices are phase-shifted from the trailing edge by 45° (to maximize thrust) and by 135° (to maximize efficiency). Optimal phases for intermediate lengths show smooth transitions between these values. The optimal motion of a body driven along its entire length is similar to that of the model tail fin driven only at its leading edge, but with an additional outward curvature near the leading edge. The similarity between optimal motions forced at the leading edge and all along the body supports the high performance attributed to fin-based motions.

Key words: propulsion, swimming/flying, vortex streets

1. Introduction

Classical works on the mechanics of fish locomotion have studied how periodic undulating motions along the fish body can generate propulsion in a quiescent inviscid fluid (Lighthill 1969; Wu 1971). In many real situations the flow is disturbed by upstream objects (including other swimming fish) before it encounters an individual swimming fish. Recently Liao *et al.* (2003) studied a trout swimming in the alternating (von Kármán) street behind an upstream D-cylinder while maintaining its streamwise distance from the D-cylinder. They observed that the trout slaloms around each oncoming vortex in the street, using a body–tail-fin swimming motion. Earlier, Streitlien, Triantafyllou & Triantafyllou (1996) had studied a computational model of a rigid aerofoil moving in an idealized von Kármán street. The foil sheds vortices in discrete clusters according to the Kutta condition of finite velocity at the trailing edge. They found that for certain parameters, the foil may gain larger thrust by moving towards the oncoming vortices instead of slaloming around them. Other experiments (Abrahams & Colgan 1987; Weimerskirch *et al.* 2001) and theoretical models (Lissaman & Shollenberger 1970; Weihs 1973; Wu & Chwang 1975) have

---

† Email address for correspondence: alben@math.gatech.edu

studied the locomotion of arrays of birds and fish and have examined the energy savings as a function of the spacings between individuals.

In Streitlien *et al.* (1996) and Liao *et al.* (2003), the swimming motion is frequency-locked to the vortex street. The motion can then be characterized by the spatial phase between the transverse displacement of the body (where it takes its maximum, or at a particular location such as the trailing edge) and the vortex street. In another work Alben (2009), we have studied the swimming of a periodic body in a vortex street. Periodic boundary conditions simplify the equations considerably and allow for exact solutions to certain optimal swimming problems and the determination of the scalings of physical quantities of interest (such as thrust force and efficiency) with respect to parameters. Forces on the body arise from the no-penetration condition, which requires the normal motion of the fluid to match the normal motion of the body. The consequent acceleration of fluid in the downstream direction provides a thrust force on the body. This periodic model neglects the important phenomenon of the shedding of vorticity by the sharp trailing edge of a finite body. Such vorticity is an important contribution to the drag forces on a finite body (Saffman 1992). For the periodic model, we have found that thrust is maximum when the phase difference between the vortices and the body motion ranges from 0° to 90°. It is 0° for a narrow vortex street and transitions smoothly to 90° when the vortex street is moderately wide (compared to the streamwise spacing between adjacent vortices).

In the present work, we consider a finite body which sheds a trailing vortex wake in accordance with the Kutta condition (Batchelor 1967; Jones 2003). We find that the optimal phase of the body motion is determined in part by the position of the trailing edge with respect to the vortices. For bodies which are short or long relative to the vortex spacing, well-defined optimal phases arise. For bodies of intermediate lengths, the optimal phase smoothly interpolates these limiting phases.

The outline of the paper is as follows. In § 2 we present the model for a finite body moving in the potential flow of the vortex street. We derive the distribution of vorticity along the body and in the wake and the distribution of pressure forces along the body. In § 3 we consider how passive and active flexible bodies (clamped or driven at the leading edge) move and obtain thrust under such pressure forcing. For small body displacements, the problem can be decomposed into three linear problems – a driven body in a uniform flow (considered previously in Alben 2008*a*), a passive elastic body (akin to a passive flag) driven by the point vortices and a beam driven at the leading edge superposed with the flow and pressure distribution of the vortex street. We determine the magnitudes of the main flow quantities; for the case of short-wavelength vortex streets, this requires re-centring the co-ordinate system at the body's trailing edge. In § 4 we consider the optimal swimming motion of a body with fully prescribed shape, in terms of the maximum thrust force and efficiency. Section 5 discusses the results in the context of previous studies.

2. Flexible body and trailing wake in a vortex street

We consider a flexible body of length $2L$ in a periodic von Kármán vortex street. The street consists of two alternating rows of vortices (see figure 1). The top row has identical point vortices, each with circulation Γ, at the points $\{ml + \mathrm{i}d/2, m \in \mathbb{Z}\}$. The bottom row has vortices with circulation $-\Gamma$ located at the points $\{(m + 1/2)l - \mathrm{i}d/2, m \in \mathbb{Z}\}$. The spacing between neighbouring vortices in a row is then l, and the width of the vortex street is d. For the von Kármán street, $\Gamma < 0$, while for the inverse von Kármán street, $\Gamma > 0$ (positive Γ corresponds to counterclockwise

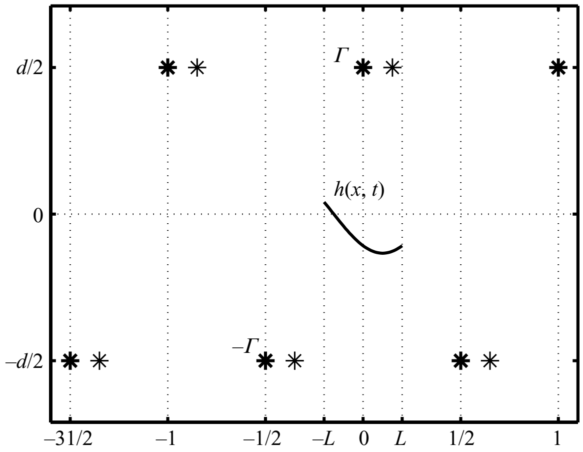

FIGURE 1. The parameters for a body of length $2L$ (solid line) swimming with amplitude $h(x,t)$ in a vortex street (bold stars) with width d and horizontal spacing between vortices l. The horizontal position of the body is assumed to be fixed (similar to that in Barrett *et al.* 1999), but the vertical deflection varies in time either passively (due to fluid forces) or actively (a prescribed vertical motion at the leading edge or all along the body, which yields a force on the body in the $-\boldsymbol{e}_x$-direction). At subsequent times the vortex street moves rightward (light stars) due to the superposition of the velocity induced by the street on itself together with a background flow velocity $U\boldsymbol{e}_x$.

rotation). We assume that the point vortices are superposed on a background flow with uniform speed U. Such is the case when vortices are shed from a stationary obstacle in a uniform stream or from an upstream body swimming at constant speed through quiescent fluid. In the latter case the background flow velocity is the negative of the upstream body velocity, when we view the vortex street in a reference frame translating with the upstream swimming body. In the unbounded plane, the vortex street translates with uniform velocity $U_c\boldsymbol{e}_x$ (Saffman 1992):

$$U_c = U + (\Gamma/2l)\tanh(\pi d/l). \tag{2.1}$$

We now introduce a body in the form of a flexible sheet along the midline between the two alternating rows of vortices. The sheet executes small-amplitude displacements $h(x,t)$ transverse to the midline and thus has complex position $x+\mathrm{i}h(x,t)$. We assume $|h| \ll d, l, L$ for the sake of analytical tractability, as explained below. We consider first the undeflected base state in which the solid sheet lies exactly along the x-axis. The condition that fluid does not penetrate the body can be satisfied by posing a vortex sheet, or equivalently a jump in tangential velocity, across the body. We also introduce a vortex-sheet wake emanating from the trailing edge of the body. The strength of the vortex-sheet wake at the trailing edge is chosen at each instant to satisfy the condition of finite flow velocity at the trailing edge – the ‘Kutta’ condition (Thwaites 1987; Bisplinghoff & Ashley 2002; Jones 2003). As a consequence, the vortex-sheet strength is continuous where the vortex wake meets the body at its trailing edge.

We now determine the unsteady strength distribution of the vortex sheet on the body and in the wake. We may use the results to compute the pressure forces on the body from the Euler equations and the deflection of a passive flexible body using the Euler–Bernoulli equation of beam bending.

When one vortex in the translating upper row of vortices crosses the y-axis (shown by the bold stars in figure 1), the flow has the following complex velocity potential (Saffman 1992):

$$w = Uz - \frac{\mathrm{i}\Gamma}{2\pi}\log\left(\sin\left(\frac{\pi}{l}\left(z - \frac{\mathrm{i}d}{2}\right)\right)\right) + \frac{\mathrm{i}\Gamma}{2\pi}\log\left(\sin\left(\frac{\pi}{l}\left(z + \frac{l}{2} + \frac{\mathrm{i}d}{2}\right)\right)\right). \quad (2.2)$$

The complex-conjugate velocity is

$$u - \mathrm{i}v = \frac{\mathrm{d}w}{\mathrm{d}z} = U - \frac{\mathrm{i}\Gamma}{2l}\cot\left(\frac{\pi}{l}\left(z - \frac{\mathrm{i}d}{2}\right)\right) + \frac{\mathrm{i}\Gamma}{2l}\cot\left(\frac{\pi}{l}\left(z + \frac{l}{2} + \frac{\mathrm{i}d}{2}\right)\right). \quad (2.3)$$

Evaluating (2.3) at $z = x$ and simplifying, we find that the point vortices induce the following velocity on the x-axis:

$$u - \mathrm{i}v\Big|_{y=0} = U - \mathrm{i}\frac{\Gamma}{l}\frac{\cosh(\pi d/l)}{\sin(2\pi x/l) - \mathrm{i}\sinh(\pi d/l)}. \quad (2.4)$$

So far we have assumed the particular instant in time at which one of the upper row of vortices crosses the y-axis. If we assume this occurs at time $t = 0$, then at subsequent times the complex velocity is given by (2.4) but with x changed to $x - U_c t$. This distribution of velocity is then a travelling wave moving with speed U_c. Separated into real and imaginary parts, the time-dependent form of (2.4) is

$$u\Big|_{y=0} = U + \frac{\Gamma}{l}\frac{\sinh(\pi d/l)\cosh(\pi d/l)}{\sin^2(2\pi(x - U_c t)/l) + \sinh^2(\pi d/l)}, \quad (2.5)$$

$$v\Big|_{y=0} = \frac{\Gamma}{l}\frac{\sin(2\pi(x - U_c t)/l)\cosh(\pi d/l)}{\sin^2(2\pi(x - U_c t)/l) + \sinh^2(\pi d/l)}. \quad (2.6)$$

We now consider the case in which $d/l \gg 1/\pi$, which includes physically reasonable vortex streets of moderate-to-large aspect ratio. Then (2.5) and (2.6) simplify to

$$u\Big|_{y=0} = u_m(1 + O(\mathrm{e}^{-2\pi d/l})), \quad u_m = U + \frac{\Gamma}{l}; \quad (2.7)$$

$$v\Big|_{y=0} = v_m(1 + O(\mathrm{e}^{-2\pi d/l})), \quad v_m(x,t) = \frac{2\Gamma}{l}\mathrm{e}^{-\pi d/l}\sin(2\pi(x - U_c t)/l). \quad (2.8)$$

We express v_m as the real part of a complex exponential:

$$v_m(x,t) = \mathrm{Re}(V_m(x)\mathrm{e}^{\mathrm{i}\omega t}); \quad V_m(x) = \frac{2\mathrm{i}\Gamma}{l}\mathrm{e}^{-\pi d/l}\mathrm{e}^{-2\pi \mathrm{i}x/l}; \quad \omega = 2\pi U_c/l. \quad (2.9)$$

The no-penetration condition on the body takes the form

$$v_m(x,t) + \frac{1}{2\pi}\int_{-L}^{L}\frac{\gamma(x',t)\mathrm{d}x'}{x - x'} + \frac{1}{2\pi}\int_{L}^{\infty}\frac{\gamma(x',t)\mathrm{d}x'}{x - \zeta(x',t)} = 0, \ -L < x < L. \quad (2.10)$$

Here $\zeta(x',t)$ is the complex position of the free vortex sheet, and we have neglected terms which are $O(h, \partial_x h)$. This equation states that on the body, the vertical flow velocity due to the point-vortex street and the body and wake vortex sheets equals the vertical velocity of the body, which is zero in the base state where the body is a flat plate.

The vortex-sheet wake $\zeta(x,t)$ is a contour in the complex plane which emanates continually from the trailing edge and is advected passively by the local fluid flow at ζ. We define the circulation in the vortex-sheet wake as an integral of the vortex-sheet strength:

$$\Gamma(x,t) = \int_{\infty}^{x} \gamma(x',t)\mathrm{d}x', \quad L < x < \infty. \tag{2.11}$$

At each material point of the vortex-sheet wake, the circulation Γ is conserved in time (Saffman 1992) and is equal to the value of circulation it had at the initiation of the material point at the trailing edge of the body at a time t^* (Krasny 1991; Jones 2003). Thus

$$\Gamma(x,t) = \Gamma(L, t^*(x)), \ L < x < \infty. \tag{2.12}$$

The initiation time t^* has a unique value for each position x on the vortex-sheet wake.

We now argue that the assumption $d/l \gg 1/\pi$ also simplifies the vortex wake dynamics and thus simplifies the last integral in (2.10). First, we note that v_m is $O(\mathrm{e}^{-\pi d/l})$. By its continuity at the trailing edge, γ is of the same order in d/l on the body and in the vortex-sheet wake. By (2.10), on both contours γ is of the same order as v_m, $O(\mathrm{e}^{-\pi d/l})$. The local fluid flow at points on the vortex-sheet wake is a superposition of four flows: the horizontal background flow U and the flows induced by the vortex sheet along the body, the vortex sheet along the wake and the point-vortex street. We assume that body is inserted into the vortex street at an initial time (t_0, say), and then the vortex-sheet wake emanates steadily under the flow at the trailing edge. The horizontal flow is u_m, and the vertical velocity there from the vortex street (v_m) and from the body's vortex sheet is $O(\mathrm{e}^{-\pi d/l})$. Thus to leading order the vortex sheet emanates horizontally from the body. At all subsequent times the horizontal velocity on the sheet is $u_m + O(\mathrm{e}^{-\pi d/l})$, and the vertical velocity remains $O(\mathrm{e}^{-\pi d/l})$. Thus for long times, at leading order in powers of $\mathrm{e}^{-\pi d/l}$ with $\pi d/l \gg 1$, we may approximate the vortex-sheet wake as a semi-infinite horizontal line extending from $x = L$ to $x = \infty$. It may be shown that the velocity induced at the point vortices in the vortex street is also $O(\mathrm{e}^{-\pi d/l})$; so we may reasonably assume (as observed in the experiment of Liao *et al.* 2003) that insertion of the body into the vortex street does not modify it at leading order.

The distribution of vorticity γ in the vortex-sheet wake is also simplified because the problem is time-periodic at leading order. The velocity of the point-vortex street equals $U_c + O(\mathrm{e}^{-\pi d/l})$ and is thus steady and horizontal at leading order. By (2.9) and (2.10) (with $\zeta(x',t) = x'$ now), the problem is periodic with a single frequency $\omega = 2\pi U_c/l$. Thus the total circulation in the wake is a periodic function:

$$\Gamma(L,t) = \Gamma_0 \mathrm{e}^{\mathrm{i}\omega t}. \tag{2.13}$$

Because the wake moves horizontally at constant speed, the distribution of circulation (and vorticity) in the vortex-sheet wake is spatially periodic:

$$\Gamma(x,t) = \Gamma(L, t^*(x)) = \Gamma\left(L, t - \frac{x-L}{u_m}\right) = \Gamma_0 \mathrm{e}^{\mathrm{i}\omega t}\mathrm{e}^{-\mathrm{i}\omega(x-L)/u_m}, L < x < \infty. \tag{2.14}$$

It is most convenient mathematically to non-dimensionalize all lengths by L (the body half-width) and time by l/U_c (the temporal period of the vortex-street motion).

Then (2.14) yields

$$\Gamma(x,t) = \Gamma_0 \mathrm{e}^{\mathrm{i}2\pi t}\mathrm{e}^{-\mathrm{i}\Omega(x-1)}, \; 1 < x < \infty, \tag{2.15}$$

$$\gamma(x,t) = \partial_x \Gamma(x,t) = G(x)\mathrm{e}^{\mathrm{i}2\pi t}, \; 1 < x < \infty, \tag{2.16}$$

$$G(x) = -\mathrm{i}\Omega\Gamma_0 \mathrm{e}^{-\mathrm{i}\Omega(x-1)}, \; 1 < x < \infty, \tag{2.17}$$

$$\Omega = \frac{\omega L}{u_m} = \frac{2\pi U_c}{u_m}\frac{L}{l} = \frac{2\pi L}{l}\frac{1+\dfrac{1}{2}(\Gamma/lU)}{1+(\Gamma/lU)}, \tag{2.18}$$

where the dependent and independent variables (including Γ_0) in (2.15)–(2.17) are now dimensionless. Equation (2.10) then becomes

$$\frac{1}{2\pi}\int_{-1}^{1}\frac{G(x')\mathrm{d}x'}{x-x'} = F(x), \quad -1 < x < 1, \tag{2.19}$$

$$F(x) = -V_m(x) - \Gamma_0 E(x), \tag{2.20}$$

$$E(x) = -\frac{\mathrm{i}\Omega}{2\pi}\int_{1}^{\infty}\frac{\mathrm{e}^{-\mathrm{i}\Omega(x'-1)}\mathrm{d}x'}{x-x'}, \tag{2.21}$$

$$V_m(x) = 2\mathrm{i}\frac{\Gamma/lU}{1+\frac{1}{2}\Gamma/lU}\frac{l}{L}\mathrm{e}^{-2\pi\mathrm{i}xL/l}\mathrm{e}^{-\pi d/l} \tag{2.22}$$

where all variables are again dimensionless. There are two unknowns to be found: Γ_0 and $G(x)$. Similar to Jones (2003), we explicitly remove the logarithmic singularity in $F(x)$ at $x = 1$:

$$F(x) = f(x) + \frac{\mathrm{i}\Omega\Gamma_0}{2\pi}\log(1-x), \tag{2.23}$$

where f is a bounded continuous function. We can solve (2.19) for G in terms of a Chebyshev expansion of f:

$$f(x) = \sum_{k=0}^{\infty} f_k \cos k\theta; \quad \theta = \arccos x. \tag{2.24}$$

The solution to (2.19) is then

$$V(\theta) = 2\sum_{k=1}^{\infty} f_k \sin k\theta \sin\theta - f_1 - 2f_0\cos\theta \tag{2.25}$$

$$+\frac{\mathrm{i}\Omega\Gamma_0}{\pi}(1-(\pi-\theta)\sin\theta + \log(2)\cos\theta) + C; \quad G(\theta) = V(\theta)/\sin\theta. \tag{2.26}$$

Here we have evaluated the Hilbert transform of $\log(1-x)$ in closed form using Mathematica 6. The constant C is set by the conservation of circulation (Kelvin's Theorem),

$$\int_{-1}^{1}\gamma(x,t)\mathrm{d}x - \Gamma(1,t) = 0, \tag{2.27}$$

which implies that $C = \Gamma_0/\pi$, using (2.26). Solution (2.26) for the bound vorticity G is continuous with the vorticity in the vortex-sheet wake at $x = 1$; both equal the real part of $-\mathrm{i}\Omega\Gamma_0 \mathrm{e}^{i2\pi t}$. We can solve for the total circulation in the wake Γ_0 explicitly using the Kutta condition that velocity (and therefore γ and G) are finite at the body's trailing edge. By (2.26) for G, V must be zero at $\theta = 0$. Then by (2.25) for V,

$$\frac{\Gamma_0}{\pi}(1+\mathrm{i}\Omega(1+\log(2))) = f_1 + 2f_0. \tag{2.28}$$

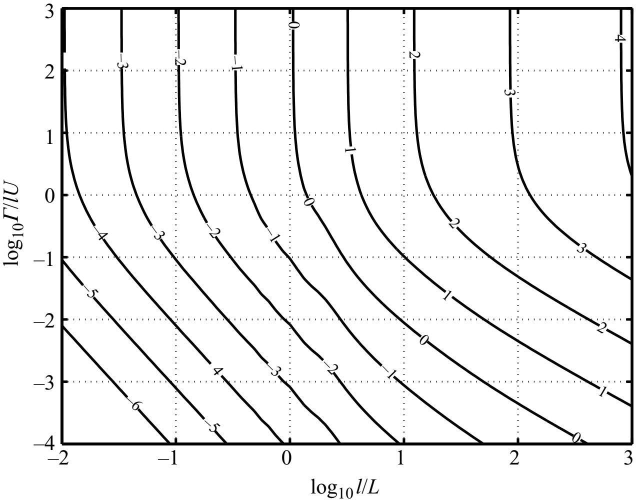

FIGURE 2. Contours of constant $\log_{10}|\Gamma_0|\mathrm{e}^{\pi d/l}$ in the space of the point vortices' strength $|\Gamma|/lU$ and their horizontal spacing l/L. The normalizing factor $\mathrm{e}^{\pi d/l}$ is included to remove dependence on d/l.

Using (2.23) and (2.20),

$$\Gamma_0 = \frac{-2\int_{-1}^{1} V_m(x)\sqrt{\dfrac{1+x}{1-x}}\mathrm{d}x}{1+\mathrm{i}\Omega(1+\log(2))+2\int_{-1}^{1}\left[E(x)+\frac{\mathrm{i}\Omega}{2\pi}\log(1-x)\right]\sqrt{\dfrac{1+x}{1-x}}\mathrm{d}x}. \tag{2.29}$$

The integrands in (2.29) are bounded when the variable of integration is changed from x to θ. In figure 2 we plot contours of the strength of the shed sheet, $|\Gamma_0|$, with respect to the strength of the vortices, $|\Gamma|/lU$, and their horizontal spacing relative to the plate length l/L. There are four asymptotic regimes which can be deduced from (2.29). The integrals in the numerator and denominator both involve weighted integrals of $\mathrm{e}^{-2\pi\mathrm{i}Lx/l}$. When $l/L \gg 1$, both integrals are $O(1)$ in l/L. Then $|\Gamma_0| \sim l/L$, from the l/L prefactor in V_m. When $l/L \ll 1$, both integrals are $O((l/L)^{-1/2})$ (shown in §3.4, (3.35)). Then $|\Gamma_0| \sim (l/L)^2$, from the l/L prefactor in V_m and the terms proportional to $\Omega \sim L/l$ in the denominator. Then $|\Gamma_0|$ has the following scalings:

$$|\Gamma_0| \sim \frac{\mathrm{e}^{-\pi d/l}|\Gamma|/lU}{1+\frac{1}{2}\Gamma/lU}\left(\frac{l}{L}\right)^2, \quad \frac{l}{L} \ll 1; \; |\Gamma_0| \sim \frac{\mathrm{e}^{-\pi d/l}|\Gamma|/lU}{1+\dfrac{1}{2}\Gamma/lU}\frac{l}{L}, \quad \frac{l}{L} \gg 1. \tag{2.30}$$

These asymptotic scalings are verified in figure 2, a contour plot of $|\Gamma_0|$ computed numerically. We have assumed that Γ/lU, if negative, is less than 2, so that advection of the vortex street is not dominated by the self-induction of the vortices relative to the background flow – which is physically reasonable for most wake flows (Batchelor 1967).

Physically, $|\Gamma_0|$ grows with $|\Gamma|/lU$ because the strength of vorticity on the body and in the wake must be strong enough to offset the flow due to the point vortices, from the no-penetration condition. When $|\Gamma|/lU$ is large, $|\Gamma_0|$ saturates because it is non-dimensionalized using the speed U_c of the point vortex street, which grows with

$|\Gamma|/lU$ when $|\Gamma|/lU$ is large; $|\Gamma_0|$ has the same linear dependence on l/L as does the normal flow V_m when l/L is large. When l/L is small, rapid oscillations in the normal flow cancel to some extent in the vorticity induced by the normal flow, and thus $|\Gamma_0|$ tends to zero as $(l/L)^2$, more rapidly than V_m.

Having solved for Γ_0 (2.29), we now have the vortex-sheet strength in the wake. Using (2.26) we also have the solution for $G(x)$, the vortex-sheet strength on the body. From (2.26), the magnitude of G is the sum of the terms with the same magnitude as V_m and the terms proportional to Γ_0. Thus the magnitude of G is the same as V_m for l/L large and small (in which case the Γ_0 terms become subdominant):

$$|G| \sim \frac{\mathrm{e}^{-\pi d/l}|\Gamma|/lU}{1+\dfrac{1}{2}\Gamma/lU}\frac{l}{L}. \tag{2.31}$$

We may derive the difference in pressure across the body in terms of γ, which is the same as the difference in fluid pressure across a generic vortex sheet, derived by Saffman (1992) using the Euler equations expressed on either side of the body. The result is

$$\frac{1}{\rho_f}\partial_s[p] = \partial_t\gamma + \partial_s((\mu-\tau)\gamma), \tag{2.32}$$

where ρ_f is the fluid density per unit area; s is arclength along the body; μ is the tangential component of the average of the fluid velocities on either side of the body; and τ is the component of the body velocity along its tangent. For a static, horizontal body lying in $-1 < x < 1$,

$$\frac{1}{\rho_f}\partial_x[p] = \partial_t\gamma + \left(U + \frac{\Gamma}{l}\right)\partial_x\gamma, \tag{2.33}$$

where we have set μ equal to the constant u_m in (2.7). We non-dimensionalize $[p]$ by $\rho_f U_c^2(L/l)^2$, and then in dimensionless form (2.33) is

$$\partial_x[p] = \partial_t\gamma + \frac{1+\Gamma/lU}{1+\dfrac{1}{2}\Gamma/lU}\frac{l}{L}\partial_x\gamma. \tag{2.34}$$

Separating out the harmonic time dependence of $[p]$,

$$[p](x,t) = P(x)\mathrm{e}^{\mathrm{i}2\pi t}, \tag{2.35}$$

(2.33) becomes

$$\partial_x P = \mathrm{i}2\pi G + \frac{1+\Gamma/lU}{1+\dfrac{1}{2}\Gamma/lU}\frac{l}{L}\partial_x G. \tag{2.36}$$

We integrate (2.36) with the boundary condition that the pressure jump vanishes at the trailing edge,

$$P\Big|_{x=1} = 0, \tag{2.37}$$

to obtain

$$P(x) = \mathrm{i}2\pi\int_1^x G(x')\,\mathrm{d}x' + \frac{1+\Gamma/lU}{1+\frac{1}{2}\Gamma/lU}\frac{l}{L}(G(x)+\mathrm{i}\Omega\Gamma_0), \tag{2.38}$$

where we have used $G(1) = -\mathrm{i}\Omega\Gamma_0$. For $l/L \ll 1$, both terms on the right-hand side of (2.38) are $O((l/L)^2)$. For $l/L \gg 1$, the second term dominates the first by $O((l/L)^2)$

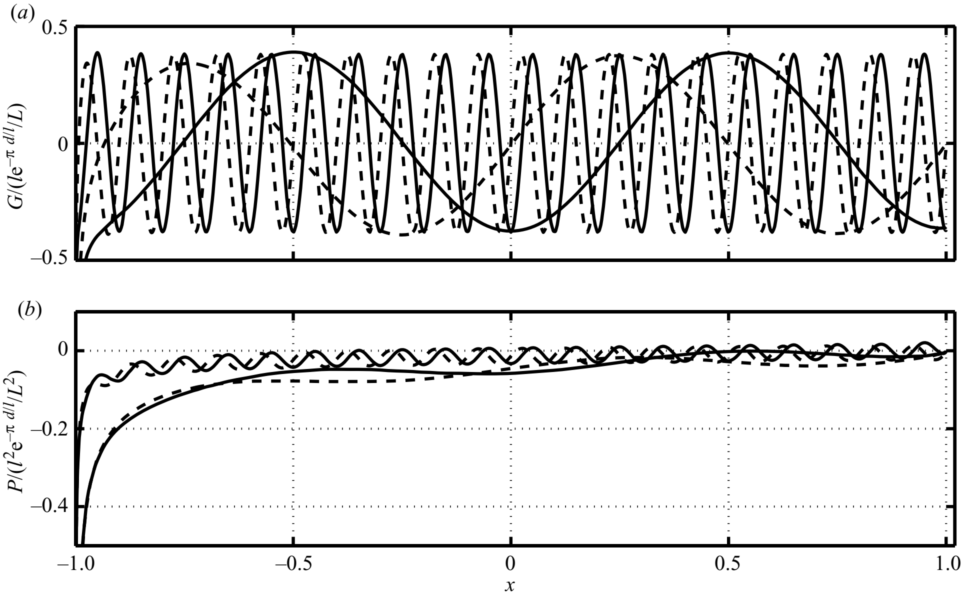

FIGURE 3. (a) The bound vorticity G and (b) the pressure P for two different values of l/L: 0.1 and 1. The wavelength of the shapes is proportional to l/L. The solid lines give the $\cos(2\pi t + \phi^{TE})$ component, and the dashed lines give the $-\sin(2\pi t + \phi^{TE})$ component, where the phase shift ϕ^{TE} (3.33) is applied to give convergence at both small and large l/L; P is multiplied by $\mathrm{e}^{\pi d/l}/(l/L)^2$ and G is multiplied by $\mathrm{e}^{\pi d/l}/(l/L)$, so the amplitudes do not change as d/l and l/L are varied. The value of $\varGamma/lU$ is 0.1. Different values of $\varGamma/lU$ mainly modify the amplitudes but not the shapes of G and P.

versus $O((l/L))$. Thus for l/L small and large,

$$|P| \sim \frac{\mathrm{e}^{-\pi d/l}|\varGamma|/lU}{1+\frac{1}{2}\varGamma/lU}\left(\frac{l}{L}\right)^2. \tag{2.39}$$

Having determined the magnitudes of $\varGamma_0$, G and P with respect to the dimensionless parameters, we now discuss the functional forms of G and P.

In figure 3 we plot G and P for small-to-moderate values of l/L. As stated previously, we are considering the regime in which $\pi d/l$ is greater than one. Here we set $\varGamma/lU = 0.1$, corresponding to a somewhat weak reverse von Kármán vortex street, and address changes due to varying $\varGamma/lU$ subsequently. Furthermore, we add a phase shift ϕ^{TE} to the functions so that the solid line in figure 3 corresponds to alignment of a vortex from the upper street with the trailing edge of the body (instead of its midpoint as for the bold stars in figure 1), and the dashed line is shifted by 90° from that phase. We have thus plotted the real and imaginary parts of $P\mathrm{e}^{\mathrm{i}\phi^{TE}}$, which converges in the limits of small l/L and large l/L, as explained further in § 3.4, (3.33) and (3.37).

For small l/L (figure 3a), G is essentially sinusoidal, apart from regions near the end points which shrink as l/L decreases. The reason that G is sinusoidal for small l/L may be seen in (2.19) and (2.20) with V_m given in (2.22). We have already noted in (2.30) that $\varGamma_0$ tends to zero like $(l/L)^2$ when l/L is small. Thus it becomes subdominant to V_m on the right-hand side of (2.19); so the flow induced by the vortex-sheet wake is subdominant to the flow induced by the point vortices, away from the ends by more than $O(l/L)$. We now recall that V_m is proportional to $\mathrm{e}^{-2\pi\mathrm{i}Lx/l}$.

Using the definition of the exponential integral with an imaginary argument $\mathrm{Ei}(ix)$ and its asymptotic behaviour for large x,

$$\int_{-1}^{1} \frac{\mathrm{e}^{\mathrm{i}kx'}\mathrm{d}x'}{x-x'} = \mathrm{e}^{\mathrm{i}kx}\left[\mathrm{i}\pi\,\mathrm{sign}(k) + \mathrm{Ei}(-\mathrm{i}k(1+x)) - \mathrm{Ei}(\mathrm{i}k(1-x))\right], \quad -1 < x < 1, \tag{2.40}$$

$$\int_{-1}^{1} \frac{\mathrm{e}^{\mathrm{i}kx'}\mathrm{d}x'}{x-x'} \sim \mathrm{e}^{\mathrm{i}kx}\left[-\mathrm{i}\pi\,\mathrm{sign}(k)\right] + O\left(\frac{1}{k}\right), \quad k \gg 1,\ 1 \pm x \gg \frac{1}{k}. \tag{2.41}$$

Equation (2.41) shows that the integral on $[-1, 1]$ behaves the same way as does the Hilbert transform on $[-\infty, \infty]$ for large k, away from small end regions. Since V_m is a complex exponential with $k = -2\pi L/l$, (2.41) shows that G has the same form for large k (small l/L):

$$G = 4\frac{\Gamma/lU}{1+\dfrac{1}{2}\Gamma/lU}\frac{l}{L}\mathrm{e}^{-2\pi\mathrm{i}Lx/l}\mathrm{e}^{-\pi d/l} + O\left(\frac{l}{L}\right)^2, 1 \pm x \gg \frac{L}{l}. \tag{2.42}$$

This form agrees well with figure 3(*a*). The asymptotic relation (2.41) may also be used to explain the good agreement between the stability diagram of a finite and an infinite flapping flag for small bending rigidity, when large-wavenumber shapes occur (Shelley, Vandenberghe & Zhang 2005; Alben 2008*b*). Furthermore, (2.41) may be used to relate vortex-sheet problems with a finite boundary to those with periodic or infinite boundary conditions (Hou, Lowengrub & Shelley 2001; Ambrose & Wilkening 2008; Alben 2009), where the Hilbert transform is simpler in Fourier space. Physically, when the wavelength of the flow on the body is much shorter than the body length, the end conditions (finite or infinite) become less important. A similar asymptotic behaviour was found in studies of a flexible body driven periodically in a fluid stream (Alben 2008*a*) and the second-order bending of a flexible fibre in a steady flow (Alben, Shelley & Zhang 2004).

We now consider the pressure at small l/L (figure 3*b*). The pressure is a linear combination of G and an integral of G (2.38). It is a sinusoidal shape superposed on a longer-wavelength background shape which diverges at the leading edge. The background shape tends to zero as l/L tends to zero, leaving a sinusoidal pressure over the whole body, except in small regions near the leading and trailing edges.

In figure 4 we show G and P at large l/L. They converge to shapes which depend on the function $E(x)$ in equation (2.21), and which are independent of l/L in this limit. The solid line in figure 4(*a*) is nearly zero away from the leading edge. This is the bound vorticity induced when the body trailing edge is aligned with a point vortex from the upper street. The near symmetry of the vortex configuration in this situation means that the normal flow is very small on the body. At the leading edge G diverges like an inverse square root, though with a small prefactor at this phase. The dashed line is nearly linear over the middle region of the body. This is the bound vorticity induced when the body trailing edge lies midway between the nearest vortices from the upper and the lower street. Then the contribution to the normal flow from the nearest vortices in each street adds constructively, yielding a maximum of bound vorticity. Because l/L is large, the normal flow is nearly uniform over the (small) body and is cancelled by a linear distribution of bound vorticity. Hence the dashed line in figure 4(*a*) is approximately linear on the central portion of the body. There is a deviation to a square-root behaviour at the trailing edge and an inverse square-root divergence at the leading edge. Because the flow from the point vortices

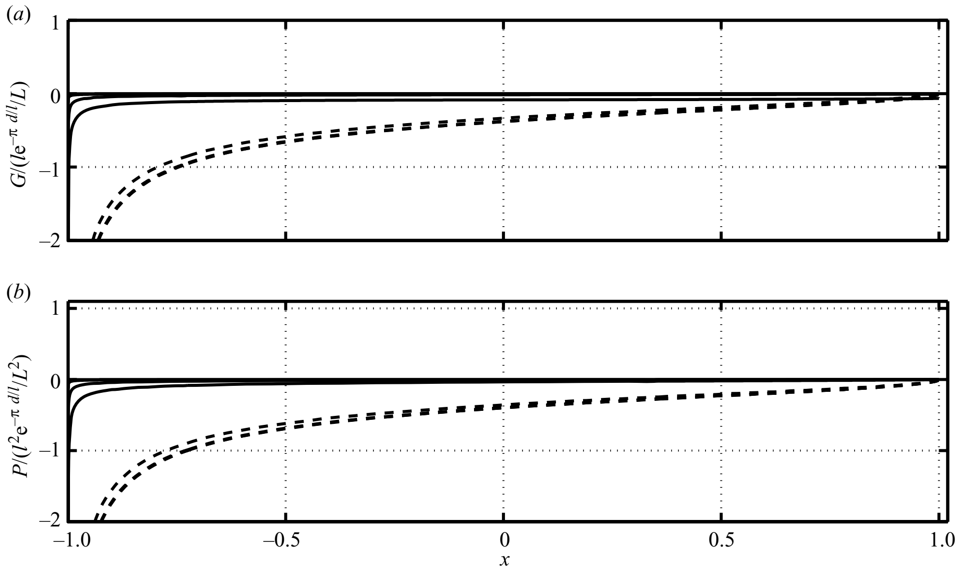

FIGURE 4. (*a*) The bound vorticity G and (*b*) the pressure P for five different values of l/L: 10 to 10^5 in integral powers of 10. Lines for the three largest values of $l/L = 10^3$, 10^4, and 10^5 show convergence to a single line which is slightly thicker than the others. The other plotting details are the same as for figure 3.

is larger in the imaginary phase than in the real phase, the prefactor of the divergence is also much larger in this case.

In figure 4(*b*), the pressure is nearly identical to the bound vorticity (figure 4*a*) times a factor of l/L. This is because the second term in (2.38) dominates the first (the integral term) for large l/L.

3. Body driven (or clamped) at the leading edge

We now consider an elastic body placed in the flow. The body is assumed to be clamped (held with zero vertical displacement and tangent angle) or driven at the leading edge and free at the trailing edge. Such a body yields a model for the tail fin of a fish swimming in a vortex street, which occurs when the fin lies in the wake of an obstacle (Liao *et al.* 2003), of another fin on the same fish (i.e. the dorsal fin; Drucker & Lauder 2001, 2005) or of another fish while swimming in a school (Weihs 1973). Because the flow induced by the vortex street is sinusoidal for wide vortex streets, this model may also be used to study the effect of generic fluid disturbances on the fin through Fourier decomposition.

The fin shape is $\zeta(x,t) = x + ih(x,t)$. We assume small deflections, so $|h|$, $|\partial_x h| \ll 1$. We also assume spatially uniform rigidity, for simplicity (but see Alben, Madden & Lauder 2007). The fin moves according to the linear beam equation and is forced by the pressure of the undisturbed vortex street:

$$R_1 \partial_{tt} h(x,t) = -R_2 \partial_{xxxx} h(x,t) - [p]. \tag{3.1}$$

Here R_1 and R_2 are the dimensionless mass per unit length and bending rigidity of the fin:

$$R_1 = \frac{\rho_s}{\rho_f L}; \quad R_2 = \frac{B}{\rho_f U_c^2 L^3}\frac{l^2}{L^2}. \tag{3.2}$$

Assuming a solution with the same temporal period as the vortex street,

$$h(x,t) = H(x)\mathrm{e}^{\mathrm{i}2\pi t}, \tag{3.3}$$

and (3.1) becomes a linear inhomogeneous ordinary differential equation (ODE):

$$-(2\pi)^2 R_1 H + R_2 \partial_{xxxx} H = -P. \tag{3.4}$$

We now assume the fin is driven at its leading edge with a combination of heaving and pitching (Lighthill 1969):

$$H(-1) = H_0 \mathrm{e}^{\mathrm{i}\phi_H}; \; H'(-1) = \Theta_0 \mathrm{e}^{\mathrm{i}\phi_\theta} \; H''(1) = H'''(1) = 0. \tag{3.5}$$

The heave and pitch amplitudes H_0 and Θ_0 are non-negative numbers. The heave and pitch phases ϕ_H and ϕ_θ give the time, in units of 2π times the period, by which the heaving or pitching maximum precedes the passage of a point vortex from the upper street over the midpoint of the body.

3.1. *Feedback from body motion on to pressure*

In §2 we derived the pressure jump P on a body which undergoes zero deflection. Now we consider how the solution to the flow–body problem, including P in (3.4), changes when the body is in motion. We assume the body deflection is no longer zero but is small ($|H|, |\partial_x H| \ll 1$). Feedback from the body motion to the flow is obtained by allowing the body motion to alter the vorticity induced on the body and in the wake and therefore also the pressure on the body. In this case, still linearized for small amplitudes, (2.10) and (2.19) are modified to read

$$\begin{aligned}(\partial_t + U\partial_x)h(x,t) = v_m(x,t) &+ \frac{1}{2\pi}\int_{-L}^{L} \frac{\gamma(x',t)\mathrm{d}x'}{x-x'} \\ &+ \frac{1}{2\pi}\int_{L}^{\infty} \frac{\gamma(x',t)\mathrm{d}x'}{x-\zeta(x',t)}, -L < x < L, \end{aligned} \tag{3.6}$$

$$\frac{1}{2\pi}\int_{-1}^{1} \frac{G(x')\mathrm{d}x'}{x-x'} = 2\pi \mathrm{i} H(x) + \frac{U}{U_c}\frac{l}{L} H'(x) - V_m(x) - \Gamma_0 E(x), \; -1 < x < 1. \tag{3.7}$$

The terms in (3.6) and (3.7) involving h and H are new, but we have neglected terms which are $O(\gamma h, \gamma \partial_x h)$. We may decompose solutions ($G_m, \Gamma_{0m}, P_m, H_m$) to the modified kinematic equation (3.7) plus the beam equation (3.4) and pressure equation (2.36) into a sum of two solutions:

$$(G_m, \Gamma_{0m}, P_m, H_m) = (G, \Gamma_0, P, H) + (G_h, \Gamma_{0h}, P_h, H_h). \tag{3.8}$$

The terms (G, Γ_0, P, H) are the solutions to (2.19) (unmodified by body motion) plus (3.4) and (2.38); ($G_h, \Gamma_{0h}, P_h, H_h$) solve the part of (3.7) with body coupling to the flow (the H terms) but without the vortex street (V_m),

$$\frac{1}{2\pi}\int_{-1}^{1} \frac{G_h(x')\mathrm{d}x'}{x-x'} = 2\pi \mathrm{i} H_h(x) + \frac{U}{U_c}\frac{l}{L} H_h'(x) - \Gamma_{0h} E(x), \quad -1 < x < 1. \tag{3.9}$$

The terms ($G_h, \Gamma_{0h}, P_h, H_h$) are then the solution for a body driven or clamped at the leading edge in a fluid stream. This problem was addressed in a previous work (Alben 2008*a*). The solutions were found to be akin to those of a damped driven oscillator, where the fluid is a source of both damping and excitation, leading to damped resonances at certain values of R_2. The only difference in H_h here is that the constant advection speed in (2.33) is now $U + \Gamma/l$ instead of U in the previous work. The structure of the solutions is essentially the same and becomes exactly the same for weak vortex streets, $\Gamma/lU \ll 1$. Thus for small deflections, the solution is a superposition of the damped-driven beam of Alben (2008*a*) with the 'decoupled' solution (G, Γ_0, P, H) in which the body is moved by the flow of a vortex street over a flat plate, but the flow is unmodified by body motion. Only the decoupled solution depends on the vortex street, and is not yet known, so we focus on it in this work. The problem of maximizing thrust or efficiency then becomes the problem of the setting the body shape to optimally 'catch the breeze' from the passing vortex street. More precisely, this means setting the body slope relative to the pressure induced by the vortex street to yield a force in the upstream direction.

The decoupled solution is also the leading-order solution in a particular asymptotic limit. In the limit that R_1 and R_2 are large relative to the magnitude of P, the body is too stiff or heavy to deflect much under the vortex pressure loading. The body shape may then be expanded as a formal asymptotic series in inverse powers of R_1 and R_2 times a function of the flow parameters d/l, l/L and Γ/lU. Although we do not pursue it further in this work, the form of this expansion can be found from the solution to the decoupled problem, which we give next.

3.2. *Body driven at the leading edge*

The solution to (3.4) with boundary conditions (3.5) is the classical variation-of-parameters solution for a linear ODE:

$$\begin{aligned} H(x) &= C_1 \mathrm{e}^{-kx} + C_2 \mathrm{e}^{kx} + C_3 \sin(kx) + C_4 \cos(kx) \\ &\quad + \frac{k^{-3}}{2R_2}\left[\frac{\mathrm{e}^{-kx}}{2}\int_{-1}^{x} \mathrm{e}^{kx'} P(x')\,\mathrm{d}x' - \frac{\mathrm{e}^{kx}}{2}\int_{-1}^{x} \mathrm{e}^{-kx'} P(x')\,\mathrm{d}x' \right. \\ &\quad \left. - \cos(kx)\int_{-1}^{x} \sin(kx')P(x')\,\mathrm{d}x' + \sin(kx)\int_{-1}^{x} \cos(kx')P(x')\,\mathrm{d}x'\right], \qquad (3.10) \\ k &= (2\pi)^{1/2}(R_1/R_2)^{1/4}. \qquad (3.11) \end{aligned}$$

Here k is the characteristic wavenumber for the neutral oscillations of an elastic rod with mass in a vacuum. The constants C_1, C_2, C_3, C_4 are chosen to satisfy the boundary conditions in (3.5) and are given in the Appendix . The solution is

$$H(x) = H_1(x) + H_2(x), \qquad (3.12)$$

a superposition of two solutions. The function $H_1(x)$ is the solution to the equation with homogeneous boundary conditions. This is the part of solution (3.10) involving P, with all the terms proportional to H_0 and Θ_0 set to zero, and is the motion of a passive body clamped at the leading edge and driven by the vortex street. The function $H_2(x)$ is the solution to the homogeneous equation

$$-(2\pi)^2 R_1 H_2 + R_2 \partial_{xxxx} H_2 = 0, \qquad (3.13)$$

with the driving boundary conditions (3.5); H_2 is the part of (3.10) involving H_0 and Θ_0, with the terms involving P set to zero.

We can quantify when the criteria $(|H| \ll 1, |\partial_x H| \ll 1)$ are met in terms of solution (3.10). For the part of the solution which depends on H_0 and Θ_0, we require that

$$H_0, \frac{\Theta_0}{k} \ll 1 \qquad (3.14)$$

for small deflections and

$$kH_0, \Theta_0 \ll 1 \qquad (3.15)$$

for small slopes. For the part of the solution which depends on P, solution (3.10) shows that body deflection magnitudes are proportional to R_1^{-1} times an integral of the pressure (with magnitude given in (2.39)). Hence the magnitude of H is

$$|H| \sim \frac{1}{R_1} \frac{\mathrm{e}^{-\pi d/l}|\Gamma|/lU}{1+\frac{1}{2}\Gamma/lU}\left(\frac{l}{L}\right)^2 . \tag{3.16}$$

Differentiating solution (3.10) introduces a factor of k; so body slope magnitudes are given by the right-hand side of (3.16) but with R_1^{-1} changed to $R_1^{-3/4}R_2^{-1/4}$. Thus for the linear theory we require

$$R_1,\ R_1^{3/4}R_2^{1/4} \gg \frac{\mathrm{e}^{-\pi d/l}|\Gamma|/lU}{1+\frac{1}{2}\Gamma/lU}\left(\frac{l}{L}\right)^2 . \tag{3.17}$$

Criteria (3.17) require the flow induced by the vortex street to be sufficiently weak relative to the body mass and rigidity. The second term on the left side of (3.17) is proportional to R_1/k. Thus, shapes of large wavenumbers are permitted provided R_1 is sufficiently large.

There is another criterion, in addition to (3.14), (3.15) and (3.17), which is necessary for the body to undergo small deflections. The resonant frequency of the body must not coincide with the frequency of the vortex street. This occurs when

$$k = 0.9376, 2.3470, 3.9273, 5.4978, \ldots, \tag{3.18}$$

where subsequent terms in the k sequence are very nearly $\pi/2$ apart (see Alben 2008*b*). These are a sequence of lines with slope 1 in the R_1–R_2 plane.

We shall now consider the motion of the clamped body as a model for a flapping flag in a vortex street. When a flag becomes unstable to flapping, small-amplitude motions grow until saturation, when nonlinear effects become important. Even for large-amplitude flapping, the small-amplitude, small-slope equations can be a reasonable approximation to the large-amplitude flag dynamics, particularly for the low-wavenumber flapping modes (Alben 2008*b*; Eloy *et al.* 2008). The model may also be applied to vortex-driven motions of stable passive bodies. The flapping-flag instability does not occur in a large region of the R_1–R_2 space, which is given approximately by the criteria that R_2 must be larger than 1 when R_1 is larger than 10 and R_2 must be larger than $0.1R_1$ when R_1 is less than 10 (Alben 2008*b*). Here R_1 is the same as in (3.2), and R_2 is the expression in (3.2) but with U_c changed to U and the factor l^2/L^2 removed.

Having described when we may expect the small-deflection theory to be valid, we now consider the motion and forces experienced by a body clamped or driven at the leading edge. In § 3.3 we consider the clamped body, given by H_1 in (3.12). Such a body yields a model for a flapping flag placed in a vortex street, which occurs when the flag lies in the wake of another object – such as a rigid obstacle (i.e. the flag pole), or another flapping flag (Ristroph & Zhang 2008), in which case $\Gamma < 0$, or a body swimming upstream, in which case $\Gamma > 0$. In § 3.4 we consider the body driven at the leading edge as a model for a flexible tail fin in a vortex street. The fin is modelled by H, a sum of H_1 and H_2 in (3.12). We shall show that the problem of optimal driving at the leading edge is one of matching the driving phases to the phases of weighted integrals of the pressure jump P.

3.3. *Small perturbations of a passive body clamped at the leading edge*

We now consider a passive elastic body, clamped at the leading edge and placed in a vortex street, given by H_1 in (3.12); H_1 may be used alone or together with H_h (in (3.8),

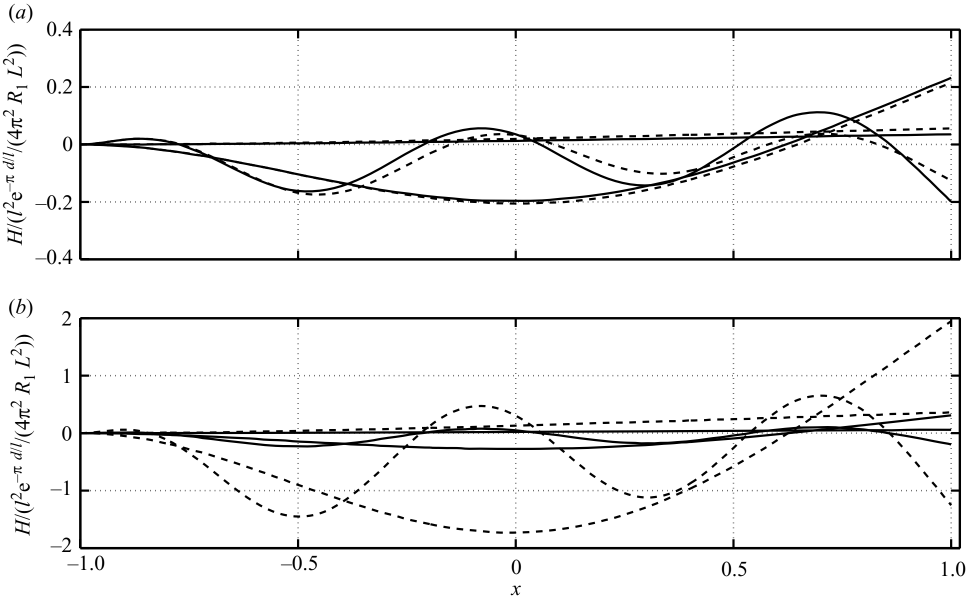

FIGURE 5. The shape of a passive flexible body for (*a*) $l/L = 1$ and (*b*) $l/L = 100$ and for $k^4/(2\pi)^2 = R_1/R_2 = 10^{-2}, 10^0, 10^2$. Larger values correspond to higher-wavenumber deformations. The solid lines give the $\cos 2\pi t$ component, and the dashed lines give the $-\sin 2\pi t$ component. Here Γ/lU is 0.1; for negative values small in magnitude, the shapes are essentially reversed in sign.

with clamped-free boundary conditions) to model a flapping flag in a vortex street. The superposition $H_h + H_1$ gives the fully coupled flapping-flag dynamics (linearized for small deflections).

Equation (3.4) is solved by H_1 solves with boundary conditions:

$$H_1(-1) = H_1'(-1) = 0\,;\; H_1''(1) = H_1'''(1) = 0. \tag{3.19}$$

In figure 5, body shapes are plotted for different values of R_1/R_2 and l/L. While the body amplitudes are proportional to $1/R_1$ (3.16), the body shapes depend only on the ratio R_1/R_2 or k, as can be seen in (3.10). The number of wavelengths on the body increases by one half as k increases through each of the intervals between resonant values (3.18); the body shape reflects across the x-axis as k moves through a resonance. Solution (3.10) shows that for both large and small l/L, the body shapes are essentially a superposition of sinusoidal waves with wavenumber k with the pressure jump. For small l/L, the sine and cosine components of the motion are nearly equal. As l/L becomes large, the sinusoidal component dominates due to the larger pressure forcing at this phase (figure 4*b*).

The instantaneous horizontal force on the body due to the flow is given by

$$F_x = -\frac{\pi}{8}v(-1,t)^2 + \int_{-1}^{1} [p](x,t)\partial_x h(x,t)\mathrm{d}x. \tag{3.20}$$

The first term on the right of (3.20) represents the suction force on the leading edge of the body (Saffman 1992) and is the limit of the pressure force on a rounded edge as the edge becomes sharp (i.e. the curvature of the edge becomes infinite). The second term on the right side of (3.20) is the horizontal component of the pressure force on the body. The period-averaged horizontal force is

$$\langle F_x \rangle = -\frac{\pi}{16}|V(-1)|^2 + \frac{1}{2}\int_{-1}^{1} \mathrm{Re}(P(x)\partial_x \bar{H}(x))\mathrm{d}x, \tag{3.21}$$

$$\langle F_x \rangle = -\frac{\pi}{16}|V(-1)|^2 + \frac{1}{2}\int_{-1}^{1} \mathrm{Re}(((2\pi)^2 R_1 H - R_2 \partial_x^4 H)\partial_x \bar{H})\mathrm{d}x, \tag{3.22}$$

$$\langle F_x \rangle = -\frac{\pi}{16}|V(-1)|^2 + \frac{1}{4}(2\pi)^2 R_1 |H|^2\Big|_1 - \frac{1}{4} R_2 |H''|^2\Big|_{-1} \tag{3.23}$$

where the bar in (3.21) denotes the complex conjugate. We have used integration by parts and the clamp boundary conditions (3.19) to simplify the equations, so only quantities at the boundaries are needed. The terms involving leading-edge suction and leading-edge curvature are negative and therefore provide thrust on the body, while the second term, involving trailing-edge deflection, is positive and thus contributes a drag force.

For a model of the flapping flag, the term H in (3.23) is a superposition of H_h and H_1. For the more quantitative discussion of forces in the remainder of this section, we now neglect the term H_h and focus instead on forces from the term H_1 due to the vortex street. Neglecting H_h is valid when the feedback from the body motion to the flow can be neglected. The feedback can be neglected when the flag is stable to flapping and when the body motion is small in amplitude and slope (inequalities (3.17) are satisfied). In this case we need only consider the contribution of H_1 to (3.23). The physical situation being considered is a passive elastic body clamped at the leading edge and is undergoing small motions due to the pressure forcing of the vortex street. Despite the limitation of small motions, the physical situation is otherwise similar to that of the unstable flag in a vortex street, and the forces may agree qualitatively in the two cases.

We begin by considering the leading-edge suction in (3.23) and relate it to the flow induced by the vortex street. Because the body motion H is induced by the fluid flow, which is $\sim G \sim V$, the suction force is of the same order as the force from body motion. Explicitly evaluating $V(-1)$ using (2.25) and the definitions of f (2.23) and F (2.20), we obtain

$$V(-1) = 4\frac{-V_{m,0} + \pi(E_0 V_{m,1} - E_1 V_{m,0})}{1 + \pi(E_1 + 2E_0)}. \tag{3.24}$$

The terms with subscripts on the right-hand side of (3.24) are the first two Chebyshev coefficients (weighted integrals) of V_m and E, defined as for f in (2.24). The leading-edge suction is essentially a weighted average of V_m, the flow induced by the vortex street.

We now set aside the leading-edge suction term, the first term on the right-hand side of (3.23), and consider the part which depends on H. Multiplying $\langle F_x \rangle$ minus the leading-edge suction by R_2,

$$\begin{aligned} R_2(\langle F_x \rangle - l.e.s.) &= \frac{1}{4}k^4 |R_2 H|^2\Big|_1 - \frac{1}{4}|R_2 H''|^2\Big|_{-1} \\ &= \left[\int_{-1}^{1} w_R(k, x')\mathrm{Re}(P(x'))\mathrm{d}x'\right]^2 + \left[\int_{-1}^{1} w_I(k, x')\mathrm{Im}(P(x'))\mathrm{d}x'\right]^2. \end{aligned} \tag{3.25}$$

Equation (3.25) is obtained by multiplying the exact solution (3.10) by R_2. The equation consists of integrals of P against weight functions w_R and w_I which depend on R_1 and R_2 only in the ratio k and not on the flow parameters l/L and Γ/lU.

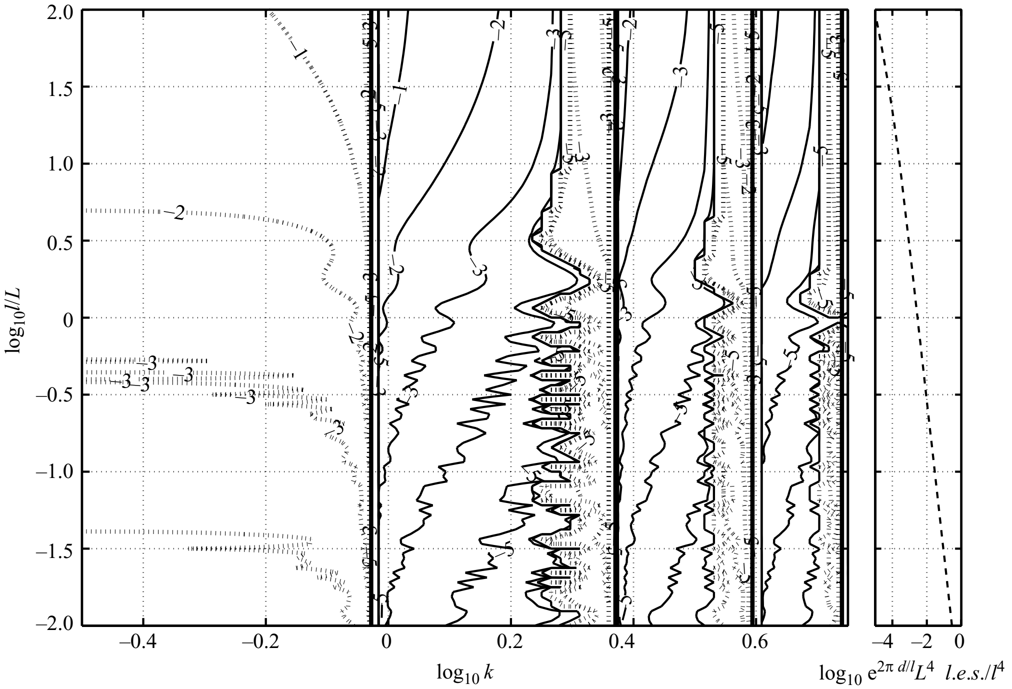

FIGURE 6. Plot of $\log_{10} R_2 e^{2\pi d/l} |\langle F_x - l.e.s.\rangle| / (R_2 (l/L)^4)$. Contours of horizontal force on a passive elastic body in a vortex street versus the wavenumber of the body, k, and the horizontal spacing of vortices, l/L. The values on each contour mark the magnitude of the force. The dotted lines mark negative force (i.e. thrust), and the solid lines mark positive force (i.e. drag). The panel to the right gives the magnitude of leading-edge suction ($l.e.s.$) versus l/L, referred to values on the vertical axis of the contour plot. Here $\Gamma/lU = 0.1$.

The average horizontal force depends on the flow parameters as the square of P. In figure 6 we plot $R_2(\langle F_x \rangle - l.e.s.)$ scaled by the magnitude of P (2.39) when l/L is large (l.e.s. is leading-edge suction). Here we assume $\Gamma/lU = 0.1$, corresponding to a vortex wake from another flapping body upstream. If instead $\Gamma/lU < 0$ (and also small in magnitude), both the pressure loading and the body slope in figure 5 are reversed in sign; so their product F_x is unchanged in sign.

We find that for the lowest mode shapes ($k < 0.93$, the first resonance), only thrust can occur. Between the first two resonances, mainly drag occurs, although there is a small region of thrust near the second resonance. Subsequent bands between the resonances show a similar pattern of drag and thrust. The reason for thrust and drag to alternate at a resonance is that the body shape, and thus its average slope, changes sign at a resonance. The horizontal force is an integral of body slope weighted by pressure.

For comparison with the pressure force on the interior of the body, on the right side of figure 6 we plot the leading-edge suction as a function of l/L. To compare these values with those in the contour plot, we must multiply the leading-edge suction by R_2. We find that for $R_2 = 1$, and $k < 2$, the leading-edge suction is dominant over the remainder of the drag at small l/L but can become subdominant at larger l/L. Increasing/decreasing R_2 makes the suction term more/less dominant. In summary, both thrust and drag can occur, depending on the wavenumber of the flag and the importance of leading-edge suction.

3.4. *Body driven at the leading edge*

We now return to the problem in which the body is driven at its leading edge with a combination of heaving and pitching. In a uniform stream, the problem was addressed in Alben (2008*a*). The body motion is given by H_2, which satisfies (3.13) with boundary conditions (3.5):

$$H_2(x) = H_0 \mathrm{e}^{\mathrm{i}\phi_H} H_{2H0}(x) + \Theta_0 \mathrm{e}^{\mathrm{i}\phi_\theta} H_{2Th0}(x), \tag{3.26}$$

$$\begin{aligned} H_{2H0}(x) = {} & \frac{\mathrm{e}^{k(x-1)}(\mathrm{e}^{2k} - \sin(2k) + \cos(2k))}{4(1+\cosh(2k)\cos(2k))} + \frac{\mathrm{e}^{k(1-x)}(\mathrm{e}^{-2k} + \sin(2k) + \cos(2k))}{4(1+\cosh(2k)\cos(2k))} \\ & + \frac{\sin(kx)}{2\coth(k)\cos(k) - 2\sin(k)} + \frac{\cos(kx)}{2\tanh(k)\sin(k) + 2\cos(k)}, \end{aligned} \tag{3.27}$$

$$\begin{aligned} H_{2Th0}(x) = {} & \frac{\mathrm{e}^{k(x-1)}(\mathrm{e}^{2k} + \sin(2k) + \cos(2k))}{4k(1+\cosh(2k)\cos(2k))} + \frac{\mathrm{e}^{k(1-x)}(-\mathrm{e}^{-2k} + \sin(2k) - \cos(2k))}{4k(1+\cosh(2k)\cos(2k))} \\ & + \frac{\sin(kx)}{-2k\tanh(k)\sin(k) + 2k\cos(k)} + \frac{\cos(kx)}{2k\coth(k)\cos(k) + 2k\sin(k)}. \end{aligned} \tag{3.28}$$

The basis functions H_{2H0} and H_{2Th0} are plotted in figure 7 for values of k midway between the first five resonances in (3.18). After the first resonance, the number of wavelengths on the functions gradually increases by one half as k increases from one resonance to the next.

The time-averaged horizontal force (3.21) in the upstream ($-x$) direction is

$$-\langle F_x \rangle = \frac{\pi}{16}|V(-1)|^2 + \mathrm{Re}\left(-\frac{1}{2}\int_{-1}^{1} \bar{P}(x)\partial_x H_1(x)\mathrm{d}x\right) \tag{3.29}$$

$$+\mathrm{Re}\left(H_0 \mathrm{e}^{\mathrm{i}\phi_H} \frac{-1}{2}\int_{-1}^{1} \bar{P}(x)\partial_x H_{2H0}(x)\mathrm{d}x\right) \tag{3.30}$$

$$+\mathrm{Re}\left(\Theta_0 \mathrm{e}^{\mathrm{i}\phi_\theta} \frac{-1}{2}\int_{-1}^{1} \bar{P}(x)\partial_x H_{2Th0}(x)\mathrm{d}x\right). \tag{3.31}$$

The first two terms – leading-edge suction and the force on a passive body – have already been considered. The two terms in the integrals on lines (3.30) and (3.31) are the forces from leading-edge motion and are proportional to the amplitudes. They are integrals of $\bar{P}$ weighted by the slopes of the basis functions H_{2H0} and H_{2Th0}. Each such integral yields a complex number. The phases ϕ_H and ϕ_θ which maximize forces are opposite to the phases of these weighted integrals of $\bar{P}$.

In figure 8 we plot the optimal phases for heaving and pitching versus the two control parameters for the model: k (body flexibility) and l/L (vortex spacing). Figure 8(*a*) is a contour plot of the optimal phase for ϕ_H, with contour lines spaced 60° apart. For k below the first resonance (at 0.93), the optimal phase converges at large l/L and oscillates rapidly at smaller l/L, shown by the many contour lines for small l/L. Figure 8(*d*) gives a contour plot of the optimal values of ϕ_θ, which also converge at large l/L and oscillate rapidly at smaller l/L.

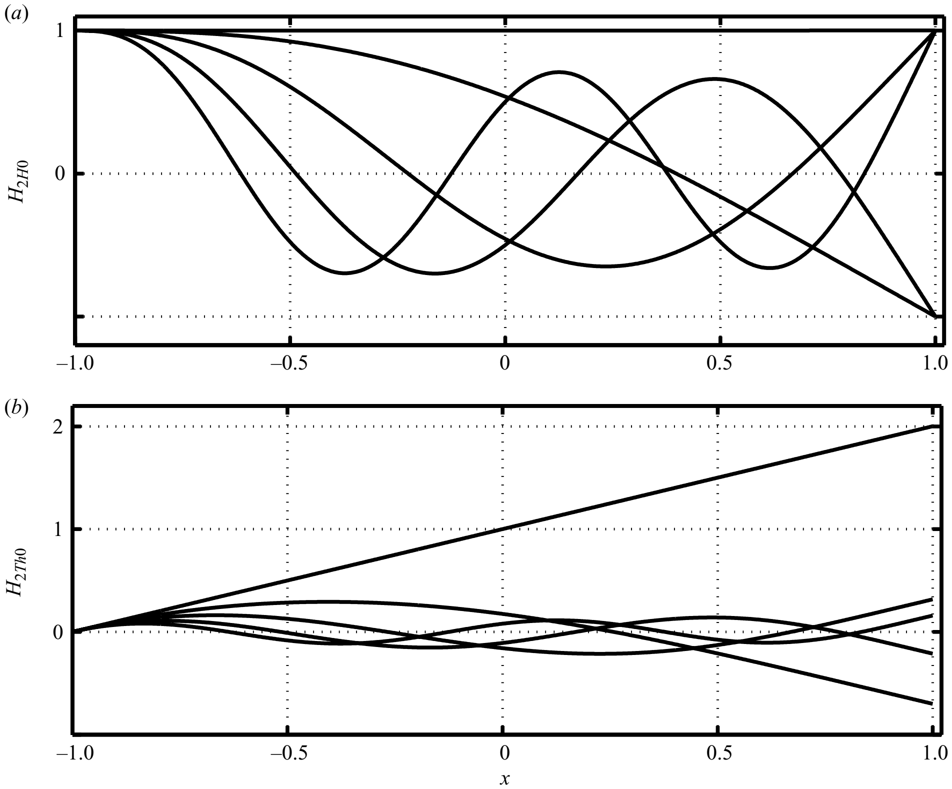

FIGURE 7. The body basis functions in (3.27) and (3.28), for values of k which are $\pi/4$ below each of the resonant values in (3.18).

The oscillation at small l/L is much reduced when we re-centre the phase. Thus far we have used the basic co-ordinate system in figure 1, where zero phase corresponds to the moment at which an upper point vortex traverses the midpoint of the body (shown by the bold stars in figure 1). We now determine the phase ϕ^{TE} when an upper point vortex traverses the 'trailing edge' in the basic co-ordinate system. We then consider the phases ϕ_H^{TE} and ϕ_θ^{TE} which are the phases of the leading-edge driving shifted by this phase ϕ^{TE}. The phases are given by

$$\phi_H^{TE} = \phi_H + \phi^{TE}, \quad \phi_\theta^{TE} = \phi_\theta + \phi^{TE}, \tag{3.32}$$

$$\phi^{TE} = 2\pi\left(\frac{L}{l} - \left\lfloor \frac{L}{l} \right\rfloor\right) \tag{3.33}$$

where $\lfloor L/l \rfloor$ denotes the largest integer less than L/l. The contour plot of the optimal ϕ_H^{TE} for thrust is plotted in figure 8(*b*) and that for ϕ_θ^{TE} is plotted in figure 8(*e*). These phases converge to the same values as figures 8(*a*) and 8(*d*) at large l/L because in this limit the body is small relative to the spacing between the vortices; so the flow and pressure on the body changes little when it is re-centred on the trailing edge of the body instead of its midpoint in the basic co-ordinate system (figure 1). At small l/L, however, the optimal ϕ_H^{TE} and ϕ_θ^{TE} show convergence instead of the rapid oscillations of ϕ_H and ϕ_θ in figures 8(*a*) and 8(*d*). We now consider the reason for

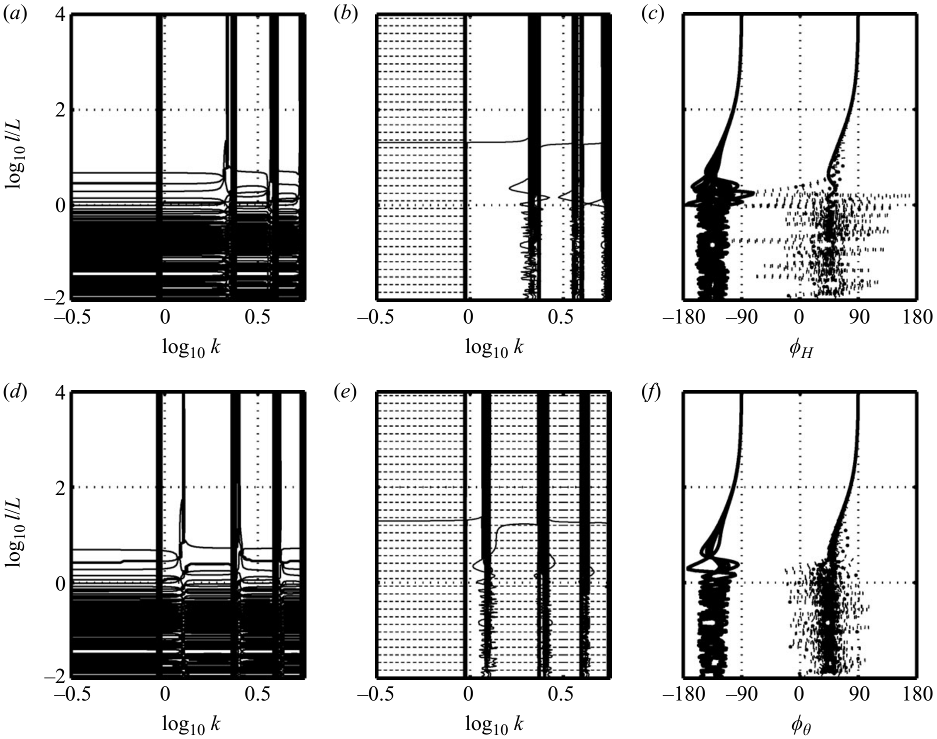

FIGURE 8. Contour plots of the optimal thrust-generating phases for (*a–c*) the driving amplitude H_0 and (*d–f*) the pitching angle Θ_0. The phase with respect to vortices in the basic co-ordinate system (figure 1) is shown in (*a*) and (*d*), and the phase with zero temporal phase reset to the instant when an upper point vortex passes the body's trailing edge is shown in (*b*) and (*e*). Each contour line corresponds to a multiple of $\pi/3$ radians. The variation of phase along vertical lines equally spaced in $\log_{10} k$ in (*b*) and (*e*) is shown in (*e*) and (*f*). The dotted lines in (*c*) and (*f*) correspond to the dotted regions in (*b*) and (*e*), and the solid lines in (*c*) and (*f*) correspond to the remaining regions in (*b*) and (*e*).

this convergence, which may be extended to explain the asymptotic scaling of Γ_0 for small l/L mentioned above (2.30).

For small l/L, there are many vortices relative to the length of the body. We can understand why the phase of the flow relative to the trailing edge converges in this limit by considering the flow in a new co-ordinate system centred on the trailing edge and with lengths scaled by l/L:

$$\tilde{x} = (1 - x)L/l. \tag{3.34}$$

Decreasing l/L in the x-frame corresponds in the $\tilde{x}$-frame to increasing the body length from the trailing edge towards the upstream direction. Because of the Kutta condition at the trailing edge of the body, the mathematical structure of the problem is determined by the flow at the trailing edge. We now show that the flow about the body converges in the $\tilde{x}$-frame in the limit that l/L goes to zero. We first consider the value of the circulation shed by the body, Γ_0 given by (2.29). We consider only the numerator, though a similar argument applies to the integral in the denominator.

The numerator is

$$-2\int_{-1}^{1} V_m(x)\sqrt{\frac{1+x}{1-x}}\mathrm{d}x = -4i\frac{l^2}{L^2}\frac{\mathrm{e}^{-\pi d/l}\Gamma/lU}{1+\frac{1}{2}\Gamma/lU}\int_0^{2/l}\mathrm{e}^{2\pi\mathrm{i}(\tilde{x}-L/l)}\sqrt{\frac{2L}{l\tilde{x}}-1}\,\mathrm{d}\tilde{x} \tag{3.35}$$

$$= -4\mathrm{i}\frac{l^2}{L^2}\frac{\mathrm{e}^{-\pi d/l}\Gamma/lU}{1+\frac{1}{2}\Gamma/lU}\mathrm{e}^{-\mathrm{i}\phi^{TE}}\int_0^{2/l}\mathrm{e}^{2\pi\mathrm{i}\tilde{x}}\sqrt{\frac{2L}{l\tilde{x}}}\,\mathrm{d}\tilde{x} + O\left(\frac{l^2}{L^2}\right). \tag{3.36}$$

$$= -2\sqrt{2}\mathrm{i}\left(\frac{l}{L}\right)^{3/2}\frac{\mathrm{e}^{-\pi d/l}\Gamma/lU}{1+\frac{1}{2}\Gamma/lU}\mathrm{e}^{-\mathrm{i}\phi^{TE}}(1+\mathrm{i}) + O\left(\frac{l^2}{L^2}\right). \tag{3.37}$$

When multiplied by $\mathrm{e}^{\mathrm{i}\phi^{TE}}$, the last term converges to a complex constant as $l/L \to 0$. The asymptotic error term in (3.37) comes from the asymptotic behaviour of the Fresnel integrals for large arguments. This argument and a similar argument applied to the denominator of Γ_0 (2.29) shows that for small l/L, the magnitude of Γ_0 grows as $(l/L)^2$ and the phase of $\Gamma_0\mathrm{e}^{\mathrm{i}\phi^{TE}}$ converges.

Inserting $\tilde{x}$ for x in (2.42), the bound vorticity G also converges to leading order in l/L, when the phase is relative to ϕ^{TE} (i.e. when G is multiplied by $\mathrm{e}^{\mathrm{i}\phi^{TE}}$). Since G and Γ_0 converge to the leading order in l/L, the pressure jump P in (2.38) also converges because the pressure jump boundary condition is applied at the trailing edge. Physically, the flow solution converges in the $\tilde{x}$-frame because as the body grows away from the trailing edge, the changes are confined to a region far from the trailing edge. Hence we obtain a convergence of the optimal driving phases ϕ_H and ϕ_θ relative to the phase of trailing edge.

We now consider the values of the optimal phases in figures 8(*b*) and 8(*e*). We shall next plot the corresponding swimming motions and use the pressure distributions induced on the body (figures 3 and 4) to understand why these motions are optimal. There are essentially two different behaviours for the optimal phases, shown by the two sets of lines in figures 8(*c*) and 8(*f*). In both panels, the solid lines converge to −90° at large l/L and to −135° at small l/L (with some oscillation about this value). The dotted lines converge to 90° at large l/L and oscillate around an average of 45° at smaller l/L. These lines give the values of the phases shown in the contour plots of figures 8(*b*) and 8(*e*). Each line gives the values of the phases versus l/L for discrete values of $\log_{10} k$ distributed equally over the range shown in figures 8(*b*) and 8(*e*). The dotted lines in figures 8(*c*) and 8(*f*) give the phase values in the dotted regions of figures 8(*b*) and 8(*e*), and the solid lines in figures 8(*c*) and 8(*f*) give the phase values in the remainder of figures 8(*b*) and 8(*e*). The phases shown by the dotted lines are essentially opposite to the phases shown by the solid lines. It may seen in figures 8(*b*) and 8(*e*) that for $10^{-0.5} < k < 1$, the optimal phase for both heaving and pitching is the same and follows the dotted-line phase. As k increases beyond the first resonance near 1, the optimal phases for heaving and pitching change by 180°, to those given by the solid lines. Shortly thereafter, the optimal phase for pitching switches back to that given by the dotted lines (figure 8*e*), while that for heaving continues to show the solid-line behaviour (figure 8*b*). We note that the size of the oscillations in the lines of figures 8(*c*) and 8(*f*) at small l/L grows as the lines approach the resonances in figures 8(*b*) and 8(*e*), which are marked by solid vertical lines. We can gain a physical understanding of the optimal phases shown in figure 8 by plotting the corresponding body trajectories. We focus on the asymptotic limits of large l/L and small l/L and small wavenumber k. Small k represents well the shapes of actual fish fins (i.e. the observations by Bainbridge 1963 of tail fins of swimming dace).

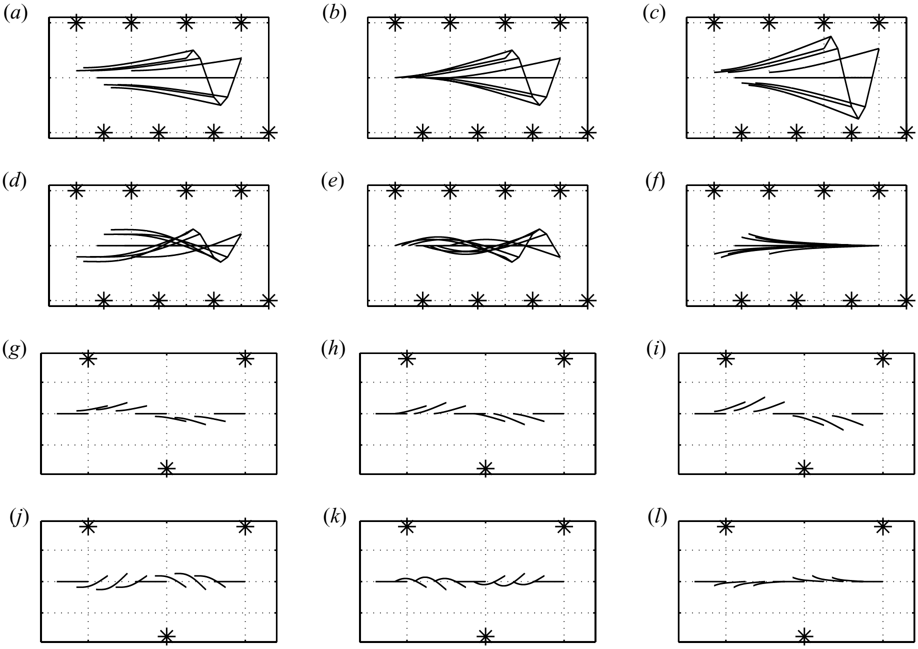

FIGURE 9. Motions of the body when the leading edge is driven with heaving and pitching at the optimal phases for thrust, as given in figures 8(*c*) and 8(*f*). Three wavenumbers and two vortex street spacings are used. The motions when $l/L=1$, small enough for the phases in figure 8 to have nearly converged in the long-body limit, are shown in (*a–f*). The motions for phases when $l/L = 10^3$, near the short-body limit, are shown in (*g–l*); in the figure $l/L = 4$ to make the bodies visible. The first column gives the motions when the optimal heaving phase is applied (without pitching). The second column gives the motions when the optimal pitching phase is applied (without heaving). The third column shows a superposition of the heaving and pitching with the same amplitudes relative to one another as in the first two columns.

In figure 9 we plot the swimming motions corresponding to the phases of heaving and pitching for maximum thrust force. The widths of the vortex streets d/l are arbitrary (but significantly larger than $1/\pi$). Figures 9(*a*)–9(*f*) are for $l/L = 1$, which is sufficiently small to approximate the behaviour of the phases in the limit of small l/L given in figures 8(*c*) and 8(*f*). We first take a body shape with $k = 0.8$, which lies in the dotted regions for both heaving and pitching in figures 8(*b*) and 8(*e*). For small l/L, the phases are 45° on average (from figures 8*c* and 8*f*). Applying heaving alone to the body with 45° phase results in the trajectories of figure 9(*a*), which are eight snapshots over a period. Instead of moving the vortices downstream with the body's streamwise position fixed as in figure 1, we move the body upstream with the vortex street fixed for visual clarity. Applying pitching alone to the body with 45° phase results in the trajectories of figure 9(*b*), which are similar to those of figure 9(*a*), but with non-zero slope at the leading edge. Superposing the trajectories of figures 9(*a*) and 9(*b*) gives those of figure 9(*c*). From the trace of the trailing edge, we see that the body's trailing edge is sloped towards the nearest vortex. At phases zero (solid line) and 90° (dashed line), figure 3 shows that there is a suction force on the side of the body facing the vortex. Since this side is also facing upstream, there is a net thrust force on the body.

The other type of optimal swimming behaviour is exemplified by that which occurs at $k = 1.7$, for which figure 8(*b*) is no longer dotted; so the heaving phase is now given by the solid lines in figure 8(*c*), opposite to that of the previous case. The optimal pitching phase remains unchanged at this value. In figures 9(*d*)–9(*f*), we give the body trajectories under heaving alone, pitching alone and heaving and pitching combined. Now the superposition of the bodies yields a shape sloped mainly at the leading edge instead of the trailing edge. The reason for this significant change in shape is that the pressure jump in figure 3(*b*) is largest at the leading edge. For each snapshot in figure 9(*e*), the slope near the leading edge is similar to that along the whole body in figure 9(*b*) – both are responsible for thrust. The now-opposite slope at the trailing edges in figure 9(*e*) subtracts relatively little from the thrust because the pressure is small near the trailing edge (figure 3*b*).

For larger l/L, the optimal phases in figures 8(*c*) and 8(*f*) increase by 45°. Since the body is relatively short, it experiences a nearly uniform flow which is maximum when the body is displaced by 90° with respect to the vortices. The corresponding pressure loading (figure 4*b*) is maximum at this phase. Because the pressure loading at 90° phase is a downward force, away from the upper vortex, the body now slopes downward for maximum thrust in figures 9(*g*)–9(*i*) when it lies 90° advanced from a vortex in the upper street. Here $k = 0.8$, and the phases are for $l/L = 10^3$, near the asymptotic limit in figure 8. In the figure l/L is only 4, however, to make the bodies visible. Figures 9(*k*)–9(*l*) show the optimal trajectories for $k = 1.7$, where the body shows a similar slope, but again confined to the leading edge, where the pressure force is largest.

Here we use $\Gamma/lU = 0.1$, a reverse von Kármán street. For a regular von Kármán street, shed by a static bluff body in a stream, Γ/lU is reversed in sign, and so is the pressure loading P and the optimal trajectories in figure 9. Thus the motions in figure 9 should be reversed for a regular von Kármán street.

The power input is the work per unit time done by the body against the fluid. Its period average is

$$\langle P_{in}\rangle = \int_0^1 \int_{-1}^1 [p](x,t)\partial_t h(x,t)\mathrm{d}x\mathrm{d}t, \tag{3.38}$$

$$\langle P_{in}\rangle = \int_0^1 \left\{ -R_2\partial_{xx}h\,\partial_{xt}h\Big|_{x=-1} + R_2\partial_{xxx}h\,\partial_t h\Big|_{x=-1} \right\} \mathrm{d}t \tag{3.39}$$

The second equation follows from the first by inserting for $[p]$ from (3.1), integrating by parts using boundary conditions (3.5) and using the time periodicity of the body motion. The second equation shows that the average power done against the fluid is also the time average of the power supplied by torque $-R_2\partial_{xx}h$ times angular velocity $\partial_{xt}h$ and normal force $R_2\partial_{xxx}h$ times normal velocity $\partial_t h$ at the leading edge.

In terms of the H and P, (3.38) reads

$$\langle P_{in}\rangle = \frac{1}{2}\int_{-1}^1 \mathrm{Re}(\bar{P}(x)2\pi\mathrm{i}H(x))\mathrm{d}x, \tag{3.40}$$

$$\langle P_{in}\rangle = \frac{1}{2}\int_{-1}^1 \left\{ H_0\mathrm{Re}(\bar{P}(x)\mathrm{e}^{\mathrm{i}\phi_H}2\pi\mathrm{i}H_{2H0}(x)) + \Theta_0\mathrm{Re}(\bar{P}(x)\mathrm{e}^{\mathrm{i}\phi_\theta}2\pi\mathrm{i}H_{2Th0}(x)) \right\} \mathrm{d}x. \tag{3.41}$$

To obtain (3.41) from (3.40), we have decomposed H into $H_1 + H_2$ as in (3.12). The contribution to (3.39) from H_1 is zero because H_1 is clamped at the leading edge. The form of (3.41) is similar to that of the average horizontal force (3.29), except that the spatial derivative of H_2 is now a time derivative.

We wish to consider swimming motions which are optimal for mechanical efficiency. One measure of efficiency is the Froude efficiency, the ratio of the output power to the input power. The output power for swimming is defined as the product of the horizontal force F_x with the horizontal swimming velocity of the body or the negative of the free-stream speed $-U$, which is non-dimensionalized by multiplying by the time scale l/U_c and dividing by the length scale L. The non-dimensional negative free-stream speed is

$$-\frac{U}{U_c}\frac{l}{L}=-\frac{1}{1+\Gamma/2lU}\frac{l}{L}. \tag{3.42}$$

A complication which arises when considering swimming in a vortex street (noted by Streitlien *et al.* 1996) is that the input power can be negative even when the thrust is positive. In other words, the pressure forces from the vortex street may put the body in a configuration yielding thrust while doing positive work on the body. Then the Froude efficiency becomes negative even though the body gains useful thrust and extracts energy from the vortices. It is more useful (as found by Streitlien *et al.* 1996) to consider the efficiency as simply the difference $\langle P_{out}\rangle-\langle P_{in}\rangle$ and determine the phases for heaving and pitching which maximize this efficiency. We thus maximize

$$\eta=-\frac{1}{1+\Gamma/2lU}\frac{l}{L}\langle F_x\rangle-\langle P_{in}\rangle, \tag{3.43}$$

where $\langle F_x\rangle$ is given in (3.21) and $\langle P_{in}\rangle$ is given in (3.41). Here the body attempts to extract energy from the street while performing a thrust-yielding motion; this energy may be used to overcome viscous forces or internal viscoelastic dissipation. We maximize the part η_{H2} of η which depends on the leading-edge driving H_2:

$$\begin{aligned}\eta_{H2}=\frac{1}{2}\int_{-1}^{1} & H_0\mathrm{Re}\left(\bar{P}(x)\mathrm{e}^{\mathrm{i}\phi_H}\left(\frac{-1}{1+\Gamma/2lU}\frac{l}{L}\partial_x H_{2H0}(x)-2\pi\mathrm{i}H_{2H0}(x)\right)\right)\\ &+\Theta_0\mathrm{Re}\left(\bar{P}(x)\mathrm{e}^{\mathrm{i}\phi_\theta}\left(\frac{-1}{1+\Gamma/2lU}\frac{l}{L}\partial_x H_{2Th0}(x)-2\pi\mathrm{i}H_{2H0}(x)\right)\right)\mathrm{d}x. \end{aligned}\tag{3.44}$$

We again consider only the optimal phases ϕ_H and ϕ_θ and assume small amplitudes H_0 and Θ_0.

In figure 10 we plot the phases of (*a*, *b*) heaving and (*c*, *d*) pitching with respect to the position of the body's trailing edge, which maximize the efficiency η_{H2}. These may be compared with figures 8(*b*), 8(*c*), 8(*e*) and 8(*f*), where thrust alone has been optimized. The patterns of contours are similar in the two cases. For large l/L, the thrust terms in (3.44) dominate, and the phases which maximize efficiency and thrust converge. For small l/L, the input power terms dominate, which leads to phase shifts of approximately ±90° between the plots in figures 8(*c*) and 8(*f*) and figures 10(*b*) and 10(*d*). The imaginary unit i in equation (3.41) is mainly responsible for this phase shift. For heaving at small l/L (figure 10*b*), the phase may be shifted up or down by 90° depending on the value of k (i.e. the shape of the body).

We have seen that the characteristic of the swimming shape which increases its output power is the correlation between the negative of its slope and the pressure jump; the characteristic which decreases input power is the correlation between the negative of the transverse velocity and the pressure jump. In figure 11 we plot the body motions corresponding to the optimal phases for efficiency, again at the values

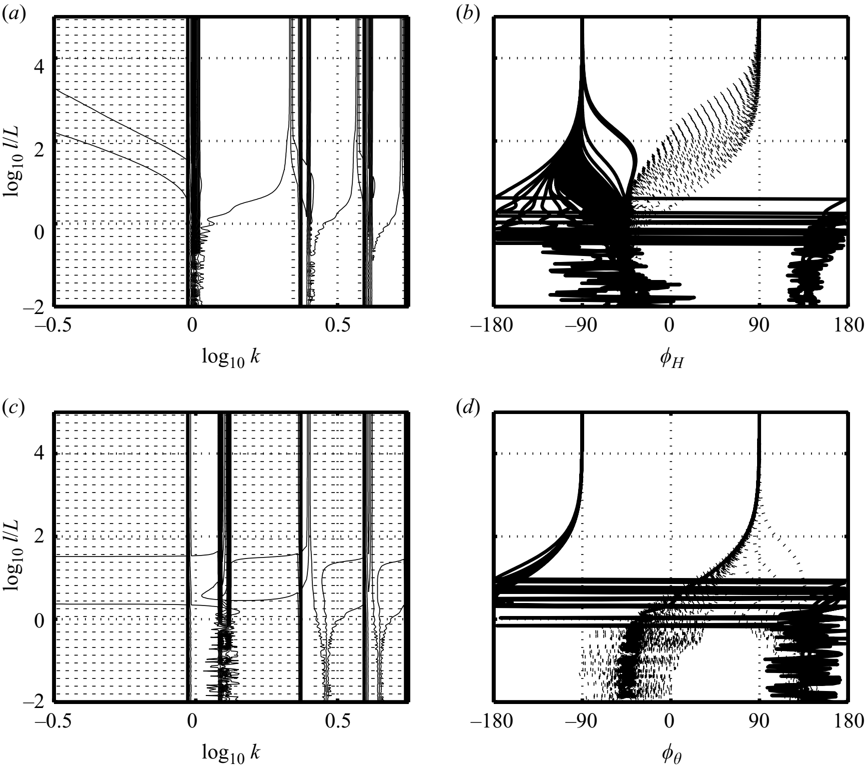

FIGURE 10. Contour plots of the optimal-efficiency phases for (*a*, *b*) the driving amplitude H_0 and (*c*, *d*) the pitching angle Θ_0. The phase with zero phase centred on the body's trailing edge is shown in (*a*) and (*c*). The variation of phase along vertical lines in (*a*) and (*c*) is shown in (*b*) and (*d*). The dotted lines give the phases for the dotted regions in (*a*) and (*c*); the solid lines give the phases in the remaining regions.

$l/L = 1$ and $l/L = 10^3$ and at the two wavenumbers $k = 0.8$ and $k = 1.7$. For small l/L, the traces of the trailing edges show that the shapes are approximately ±90° apart from those in figure 9 in phase.

For $k = 0.8$ and $l/L = 1$ (first row of figure 11), heaving and pitching motions add constructively and yield a body motion which is delayed in phase by 90° from that in the first row of figure 9. The body is still sloped upward in the first frame, when there is a suction force on its upper face yielding thrust. Because of the phase shift from figure 9, its velocity is also upward in the first frame; so it extracts energy from the upward suction force. When the pressure force has changed sign 90° later in the period, the body is now moving downward with large velocity. Hence it obtains thrust and extracts energy from the vortex street. For $k = 1.7$ (second row of figure 11) the body deflection and slope are nearly the opposite of those in the first row near the trailing edge but nearly the same near the leading edge. Because the pressure forces are largest near the leading edge, the leading edge determines the motion. At large l/L, the output power dominates the input power in the efficiency (3.44); so the third and fourth rows of figure 11 are essentially the same as in figure 9. As before, these motions correspond to a reverse von Kármán street, with $\Gamma/lU = 0.1$. For a regular von Kármán street, the motions should be inverted about the centreline.

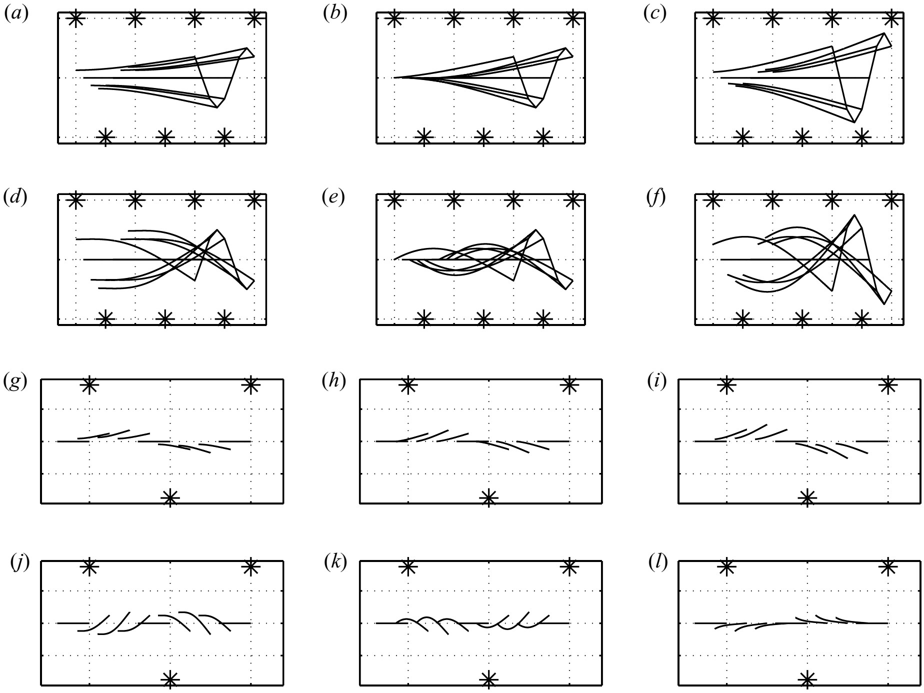

FIGURE 11. Motions of the body when the leading edge is driven with heaving and pitching at the optimal phases for efficiency, as given in figures 10(*b*) and 10(*d*). Two different wavenumbers and two difference vortex street spacings are shown. The motions when $l/L = 1$, small enough for the phases in figure 10 to have nearly converged in the long-body limit, are shown in (*a*)–(*f*). The motions in the limit of large l/L are shown in (*g*)–(*l*). The first column gives the motions when the optimal heaving phase is applied (without pitching). The second column gives the motions when the optimal pitching phase is applied (without heaving). The third column superposes motions from the first two columns, with the same relative amplitudes as in the first two columns. Here we assume a reverse von Kármán street, $\Gamma/lU = 0.1$.

4. Body driven along its length

We now apply (3.21) to a body with motion prescribed everywhere along its length. In general the optimization problem will not have a solution unless constraints are applied to enforce a given amplitude or smoothness of the motion (Sparenberg 1995).

We first consider the body motion which maximizes average thrust for a given (small) mean amplitude. Fixing the time-averaged amplitude of deflection to be A, the Lagrangian and its variation are

$$L = -\langle F_x\rangle - \lambda\left(\frac{1}{4}\int_{-1}^{1}|H|^2\mathrm{d}x - A^2\right), \tag{4.1}$$

$$\delta L = \frac{1}{2}\int_{-1}^{1}(-P_R\delta H_R' - P_I\delta H_I' - \lambda(H_R\delta H_R + H_I\delta H_I))\mathrm{d}x, \tag{4.2}$$

$$\delta L = -\frac{1}{2}(P_R\delta H_R + P_I\delta H_I)\Big|_{-1}^{1} + \frac{1}{2}\int_{-1}^{1}((P_R' - \lambda H_R)\delta H_R + (P_I' - \lambda H_I)\delta H_I)\,\mathrm{d}x. \tag{4.3}$$

The solution to the variational equation is

$$H = AP' \Big/ \left(\frac{1}{2}\int_{-1}^{1} |P'|^2 \mathrm{d}x\right)^{1/2}. \tag{4.4}$$

Because P behaves like an inverse square root of distance from the leading edge and a square root of distance from the trailing edge, the integral in the denominator of (4.4) is divergent at both endpoints.

A simple alternative constraint is to fix the mean square of the slope, which means replacing H in (4.1) by H'. Fixing the mean-square slope also bounds the maximum displacement $|H|$ (since displacement is the integral of the slope). The Lagrangian becomes

$$L_1 = -\langle F_x \rangle - \lambda \left(\frac{1}{4}\int_{-1}^{1} |H'|^2 \mathrm{d}x - A_1^2\right), \tag{4.5}$$

$$\delta L_1 = \frac{1}{2}\int_{-1}^{1} (-P_R \delta H_R' - P_I \delta H_I' - \lambda(H_R' \delta H_R' + H_I' \delta H_I'))\,\mathrm{d}x, \tag{4.6}$$

$$\begin{aligned}\delta L_1 = &-\frac{1}{2}((P_R + \lambda H_R')\delta H_R + (P_I + \lambda H_I')\delta H_I)\Big|_{-1}^{1} \\ &+ \frac{1}{2}\int_{-1}^{1} ((P_R' + \lambda H_R'')\delta H_R + (P_I' + \lambda H_I'')\delta H_I)\,\mathrm{d}x.\end{aligned} \tag{4.7}$$

Before stating the solution we note that it is also possible to constrain the mean-square curvature, which is related to the internal viscous damping in the body (such as that due to internal connective tissue (Cheng, Pedley & Altringham 1998; Alben 2009).

The minimizer of L_1 is

$$H_{A1} = -\frac{1}{\lambda}\int_{-1}^{x} P(x) + c_1 x + c_0, \tag{4.8}$$

where c_1 and c_0 are constants set by the free boundary conditions on H, given by setting the coefficients of boundary terms in (4.7) to zero. These conditions imply $c_1 = 0$. The constant c_0 does not affect L_1, so it is arbitrary. We set it by setting the average of H_1 equal to zero, consistent with small displacements. The solution H_1 then becomes

$$H_{A1} = -A_1 \left(\int_{-1}^{x} P - \frac{1}{2}\int_{-1}^{1} \mathrm{d}x \int_{-1}^{x} P \mathrm{d}x'\right) \Big/ \left(\frac{1}{4}\int_{-1}^{1} |P|^2 \mathrm{d}x\right)^{1/2}. \tag{4.9}$$

The average thrust force corresponding to H_{A1} is

$$-\langle F_x \rangle = -\frac{1}{2}\int_{-1}^{1} \mathrm{Re}(\bar{P}(x) H_{A1}'(x))\mathrm{d}x = 2A_1. \tag{4.10}$$

If $H_{A1}(x) + f(x)$ is another body motion which has mean-square slope equal to A_1, i.e.

$$\frac{1}{4}\int_{-1}^{1} |H_{A1}' + f'|^2 \mathrm{d}x = A_1^2, \tag{4.11}$$

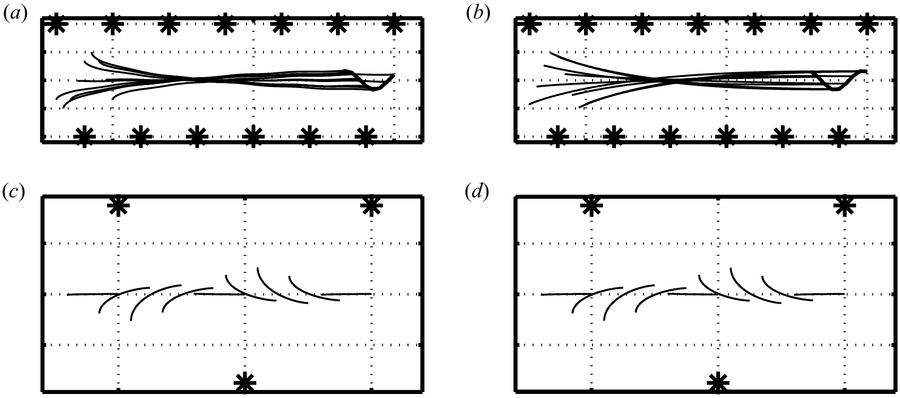

FIGURE 12. (*a*, *c*) Swimming shapes which optimize thrust (4.9) or (*b*, *d*) efficiency (4.15), for fixed mean slope. Here (*a*, *b*) l/L=0.4 or (*c*, *d*) $l/L = 10^3$.

then the average thrust force is

$$-\langle F_x\rangle = -\frac{1}{2}\int_{-1}^{1}\mathrm{Re}(\bar{P}(x)(H'_{A1}+f'))\mathrm{d}x = 2A_1 - \frac{\left(\frac{1}{4}\int_{-1}^{1}|P|^2\mathrm{d}x\right)^{1/2}}{4A_1}\int_{-1}^{1}|f'|^2\mathrm{d}x, \tag{4.12}$$

which is clearly less than $2A_1$ for non-zero f. The final expression in (4.12) follows by substituting a term proportional to H'_{A1} for P in the middle expression, using (4.9) and the slope constraint (4.11).

The Lagrangian corresponding to (4.6) for maximum efficiency is given by

$$L_{1\mathrm{e}} = \frac{1}{2}\int_{-1}^{1}\mathrm{Re}\left(\bar{P}\left(\frac{-1}{1+\Gamma/2lU}\frac{l}{L}\partial_x H - 2\pi \mathrm{i} H\right)\right)\mathrm{d}x - \lambda\left(\frac{1}{4}\int_{-1}^{1}|H'|^2\mathrm{d}x - A_1^2\right), \tag{4.13}$$

$$\begin{aligned}\delta L_{1\mathrm{e}} = {} & \frac{1}{2}\left(\left(\frac{-1}{1+\Gamma/2lU}\frac{l}{L}P_R - \frac{\lambda}{2}H'_R\right)\delta H_R + \left(\frac{-1}{1+\Gamma/2lU}\frac{l}{L}P_I - \frac{\lambda}{2}H'_I\right)\delta H_I\right)\Big|_{-1}^{1} \\ & - \frac{1}{2}\int_{-1}^{1}\left(\left(\frac{-1}{1+\Gamma/2lU}\frac{l}{L}P'_R - \frac{\lambda}{2}H''_R + 2\pi P_I\right)\delta H_R \right. \\ & \left. + \left(\frac{-1}{1+\Gamma/2lU}\frac{l}{L}P'_I - \frac{\lambda}{2}H''_I - 2\pi P_R\right)\delta H_I\right)\mathrm{d}x. \end{aligned} \tag{4.14}$$

The solution is

$$\frac{\lambda}{2}H = -\int_{-1}^{x}\frac{1}{1+\Gamma/2lU}\frac{l}{L}P\,\mathrm{d}x' - 2\pi\mathrm{i}\int_{-1}^{x}\int_{-1}^{x'}P\,\mathrm{d}x''\mathrm{d}x' + c_0, \tag{4.15}$$

where constant λ is set so that H has mean-square slope equal to A_1. The free constant c_0 can be chosen to decrease the input power without affecting the constraint. An additional constraint is thus required to fix c_0. Perhaps the simplest constraint is the same as was used for H_{A1} (4.9), which is to make the mean displacement of the body zero. We thus focus attention on the particular shape the body assumes but not its mean heaving motion.

In figure 12 we plot optimal swimming shapes for $l/L = 0.4$ and 10^3, values in the asymptotic regimes of § 3.4. For small l/L, the optimal thrust shape (figure 12*a*) agrees well with those in the first row of figure 9. There is an additional curvature near the leading edge here, due to the large pressure there. The optimal-efficiency shape (figure 12*b*) resembles those in the first row of figure 11, in terms of the phase of the trailing-edge motion relative to the vortices; it is closest in wavenumber to these slightly flexed plates. Again, a larger slope is seen at the leading edge to take advantage of the larger pressure there. For larger l/L, the optimal thrust motion (figure 12*c*) has a slope similar to those in figures 9 and 11, but here there is no net heaving motion. The shapes now have large curvatures to take advantage of large thrust near the leading edge.

5. Conclusion

We have studied optimal swimming of a finite body in a vortex street in the limit of small body motions, where the linearized theory is valid. In § 2 we have computed the distribution of vorticity and pressure in the flow with respect to the strength of the vortex street relative to the background flow (Γ/lU) and the streamwise spacing of the vortices relative to the body half-length (l/L). The vorticity on the body is sinusoidal away from the body ends for a long body ($l/L \ll 1$) and is roughly linear away from the ends for a short body, when the body is between vortices, and nearly zero when the body coincides with a vortex in streamwise position. The pressure loading on the body is also oscillatory away from the ends for $l/L \ll 1$ and is nearly proportional to the bound vorticity for $l/L \gg 1$.

We have studied two models for the body. In the first (§ 3), the body is clamped or oscillated at the leading edge. The input and output forces are computed with respect to body mass R_1 and flexibility R_2. The clamped body models a passive elastic body (such as a flapping flag) in a vortex wake. The vortices cause thrust at the lowest wavenumber mode and alternating thrust and drag in higher modes. These body motions may be linearly superposed with the flag in a uniform stream to obtain the effect of the vortex street for the fully coupled problem. The body driven at the leading edge is a model for the tail fin of a swimming fish. We identify optimal phases for heaving and pitching motions of the body which have clear limiting values at small l/L and large l/L, when phase is measured with respect to the alignment of the trailing edge with an upper vortex. For short bodies maximizing thrust or efficiency, we find deflections away from oncoming vortices in a reverse von Kármán street and towards oncoming vortices in a regular von Kármán street. For long bodies, optimal motions at the trailing edge are phase-shifted from those for a short body by 45° when thrust is maximized and by 135° when efficiency is maximized. Optimal phases for intermediate lengths interpolate these values smoothly.

In the second model for the body (§ 4), its motion is prescribed along its length. We identify optimal swimming motions for maximum thrust and efficiency, subject to a constraint of fixed mean body slope. We find shapes which are similar to the lowest wavenumber shapes driven at the leading edge, but with an additional upward slope near the leading edge. This indicates that a body driven only at one end may obtain a performance nearly as good as a body driven all along its length. In applications to fish swimming, this supports the more frequent utilization of tail-fin swimming (carangiform and sub-carangiform) over whole-body (anguilliform) swimming, for which internal viscous energy losses are larger (Lighthill 1969).

Liao *et al.* (2003) observed trout slaloming around the vortices of an oncoming von Kármán street in their experiment. The leading edge of the trout body led the passage of vortices by approximately 100° in phase (on average), while for the trailing edge the phase was 240° and for the midpoint 180°. Also, muscle activity was concentrated near the leading edge of the body, similar to the model of a body driven passively at the leading edge in § 3. In the present work, the model most similar to this situation is the body driven all along its length (§ 4). In the model, the pressure forces near the leading edge is dominant, and the motion of the leading edge is close in phase (ranging from 80° to 100°) to that observed by Liao and Lauder, for both the optimum thrust and optimum efficiency shapes and l/L of order 1. The phase at the trailing edge varies over a wider range in the model. By contrast, the heaving and pitching rigid aerofoil studied by Streitlien and Triantafyllou (Streitlien *et al.* 1996) generally showed larger lift and thrust when the leading edge of the aerofoil moved at nearly zero phase relative to the oncoming vortex street. The reason may be that at large heaving amplitudes, the aerofoil can be sensitive to the singular velocity near the point vortex.

This work was supported by the National Science Foundation Division of Mathematics Sciences, grant NSF-DMS-0810602.

Appendix. Constants in driven (or clamped) fin solution

The constants C_1, C_2, C_3, C_4 in (3.10) are

$$C_1 = -\frac{\mathrm{e}^{-k}}{4k^3}\frac{I_2 D_1 - I_1 D_2 + k^2\mathrm{e}^{2k} D_3 \Theta_0 - k^3 \mathrm{e}^{2k} D_4 H_0}{F_1}, \tag{A 1}$$

$$C_2 = \frac{\mathrm{e}^{k}}{4k^3}\frac{k^2 D_1 \Theta_0 + k^3 H_0 D_2 + \mathrm{e}^{2k} D_3 I_2 + \mathrm{e}^{2k} D_4 I_1}{F_1}, \tag{A 2}$$

$$C_3 = \frac{1}{2k^3}\frac{(-I_2 + k^2\Theta_0)\cosh k + (I_1 + k^3 H_0)\sinh k}{F_2}, \tag{A 3}$$

$$C_4 = \frac{1}{2k^3}\frac{(I_2 + k^2\Theta_0)\sinh k + (-I_1 + k^3 H_0)\cosh k}{F_3}, \tag{A 4}$$

$$D_1 = \mathrm{e}^{2k} + \sin(2k) + \cos(2k), \tag{A 5}$$

$$D_2 = \mathrm{e}^{2k} - \sin(2k) + \cos(2k), \tag{A 6}$$

$$D_3 = \mathrm{e}^{-2k} - \sin(2k) + \cos(2k), \tag{A 7}$$

$$D_4 = \mathrm{e}^{-2k} + \sin(2k) + \cos(2k), \tag{A 8}$$

$$F_1 = 1 + \cosh(2k)\cos(2k), \tag{A 9}$$

$$F_2 = \cosh(k)\cos(k) - \sinh(k)\sin(k), \tag{A 10}$$

$$F_3 = \cosh(k)\cos(k) + \sinh(k)\sin(k), \tag{A 11}$$

$$I_1 = -\frac{1}{2R_2}\left[\frac{\mathrm{e}^{-k}}{2}\int_{-1}^{1}\mathrm{e}^{kx'}P(x')\mathrm{d}x' - \frac{\mathrm{e}^{k}}{2}\int_{-1}^{1}\mathrm{e}^{-kx'}P(x')\mathrm{d}x'\right. \tag{A 12}$$

$$\left. + \cos(k)\int_{-1}^{1}\sin(kx')P(x')\mathrm{d}x' - \sin(k)\int_{-1}^{1}\cos(kx')P(x')\mathrm{d}x'\right], \tag{A 13}$$

$$I_2 = -\frac{1}{2R_2}\left[-\frac{\mathrm{e}^{-k}}{2}\int_{-1}^{1}\mathrm{e}^{kx'}P(x')\mathrm{d}x' - \frac{\mathrm{e}^{k}}{2}\int_{-1}^{1}\mathrm{e}^{-kx'}P(x')\mathrm{d}x'\right. \tag{A 14}$$

$$\left. - \sin(k)\int_{-1}^{1}\sin(kx')P(x')\mathrm{d}x' - \cos(k)\int_{-1}^{1}\cos(kx')P(x')\mathrm{d}x'\right]. \tag{A 15}$$

REFERENCES

Abrahams, M. V. & Colgan, P. W. 1987 Fish schools and their hydrodynamic function: a reanalysis. *Environ. Biol. Fishes* **20** (1), 79–80.

Alben, S. 2008*a* Optimal flexibility of a flapping appendage at high Reynolds number. *J. Fluid Mech.* **614**, 355–380.

Alben, S. 2008*b* The flapping-flag instability as a nonlinear eigenvalue problem. *Phys. Fluids* **20**, 104–106.

Alben, S. 2009 On the swimming of a flexible body in a vortex street. *J. Fluid Mech.* **635**, 27–45.

Alben, S., Madden, P. G. & Lauder, G. V. 2007 The mechanics of active fin-shape control in ray-finned fishes. *J. R. Soc. Interface* **4** (13), 243–256.

Alben, S., Shelley, M. & Zhang, J. 2004 How flexibility induces streamlining in a two-dimensional flow. *Phys. Fluids* **16**, 1694.

Ambrose, D. M. & Wilkening, J. 2008 Global paths of time-periodic solutions of the Benjamin–Ono equation connecting arbitrary travelling waves. Preprint. ArXiv:0811.4205.

Bainbridge, R. 1963 Caudal fin and body movement in the propulsion of some fish. *J. Exp. Biol.* **40** (1), 23–56.

Barrett, D. S., Triantafyllou, M. S., Yue, D. K. P., Grosenbaugh, M. A. & Wolfgang, M. J. 1999 Drag reduction in fish-like locomotion. *J. Fluid Mech.* **392**, 183–212.

Batchelor, G. K. 1967 *An Introduction to Fluid Dynamics*. Cambridge University Press.

Bisplinghoff, R. L. & Ashley, H. 2002 *Principles of Aeroelasticity*. Dover.

Cheng, J.-Y., Pedley, T. J. & Altringham, J. D. 1998 A continuous dynamic beam model for swimming fish. *Phil. Trans. R. Soc. Lond* B **353**, 981–997.

Drucker, E. G. & Lauder, G. V. 2001 Locomotor function of the dorsal fin in teleost fishes: experimental analysis of wake forces in sunfish. *J. Exp. Biol.* **204** (17), 2943–2958.

Drucker, E. G. & Lauder, G. V. 2005 Locomotor function of the dorsal fin in rainbow trout: kinematic patterns and hydrodynamic forces. *J. Exp. Biol.* **208** (23), 4479–4494.

Eloy, C., Lagrange, R., Souilliez, C. & Schouveiler, L. 2008 Aeroelastic instability of cantilevered flexible plates in uniform flow. *J. Fluid Mech.* **611**, 97–106.

Hou, T. Y., Lowengrub, J. S. & Shelley, M. J. 2001 Boundary integrals methods for multicomponent fluids and multiphase materials. *J. Comput. Phys.* **169**, 302–362.

Jones, M. 2003 The separated flow of an inviscid fluid around a moving flat plate. *J. Fluid Mech.* **496**, 405–441.

Krasny, R. 1991 Vortex sheet computations: roll-up, wakes, separation. *Lect. Appl. Math.* **28**, 385–402.

Liao, J. C., Beal, D. N., Lauder, G. V. & Triantafyllou, M. S. 2003 Fish exploiting vortices decrease muscle activity. *Science* **302** (5650), 1566–1569.

Lighthill, J. M. 1969 Hydromechanics of aquatic animal propulsion. *Annu. Rev. Fluid Mech.* **1**, 413–446.

Lissaman, PBS & Shollenberger, C. A. 1970 Formation flight of birds. *Science* **168** (3934), 1003–1005.

Ristroph, L. & Zhang, J. 2008 Anomalous hydrodynamic drafting of interacting flapping flags. *Phys. Rev. Lett.* **101** (19), 194502.

Saffman, P. 1992 *Vortex Dynamics*. Cambridge University Press.

Shelley, M., Vandenberghe, N. & Zhang, J. 2005 Heavy flags undergo spontaneous oscillations in flowing water. *Phys. Rev. Lett* **94**, 094302.

Sparenberg, J. A. 1995 *Hydrodynamic Propulsion and Its Optimization: Analytic Theory*. Springer.

Streitlien, K., Triantafyllou, G. S. & Triantafyllou, M. S. 1996 Efficient foil propulsion through vortex control. *AIAA J.* **34** (11), 2315–2319.

Thwaites, B. 1987 *Incompressible Aerodynamics: An Account of the Theory and Observation of the Steady Flow of Incompressible Fluid Past Aerofoils, Wings and Other Bodies*. Dover.

Weihs, D. 1973 Hydromechanics of fish schooling. *Nature* **241** (5387), 290–291.

Weimerskirch, H., Martin, J., Clerquin, Y., Alexandre, P. & Jiraskova, S. 2001 Energy saving in flight formation. *Nature* **413** (6857), 697–698.

Wu, T. Y. 1971 Hydromechanics of swimming propulsion. Part 1. Swimming of a two-dimensional flexible plate at variable forward speeds in an inviscid fluid. *J. Fluid Mech.* **46** (2), 337–355.

Wu, T. Y. & Chwang, A. T. 1975 Extraction of flow energy by fish and birds in a wavy stream. In *Swimming and Flying in Nature* (ed. T. Y.-T. Wu, C. J. Brokaw & C. Brennen), vol. 2, pp. 687–702. Plenum.